MR3252: Tropical Meteorology

Mesoscale Convective Systems in the Tropics

Main Topics:

- Vertical modes of heating
- Convective and stratiform precipitation

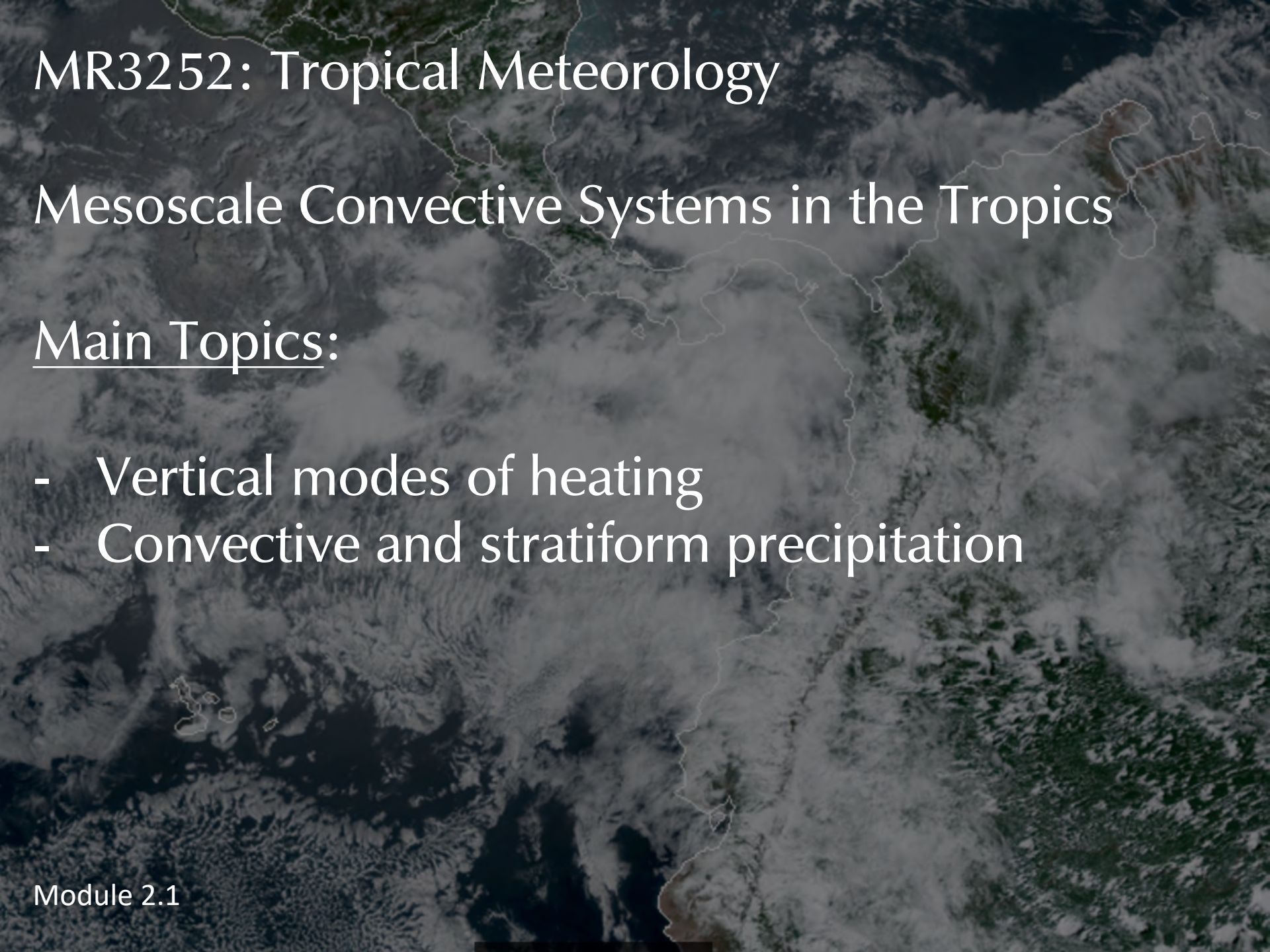

Module 2.1

Mesoscale Convective Systems (MCSs) are regions of contiguous precipitation of ~100 km or more in horizontal dimension.

Much of the deep convection in the Tropics (and therefore the rainfall) come from MCSs.

About 50% of cirrus cloud in the Tropics originates as part of an MCS.

MCSs consist of **convective** and **stratiform** regions of precipitation and represent a mature stage of the convective lifecycle.

Shallow-to-deep transition of convection requires conditional instability and sufficient moisture.

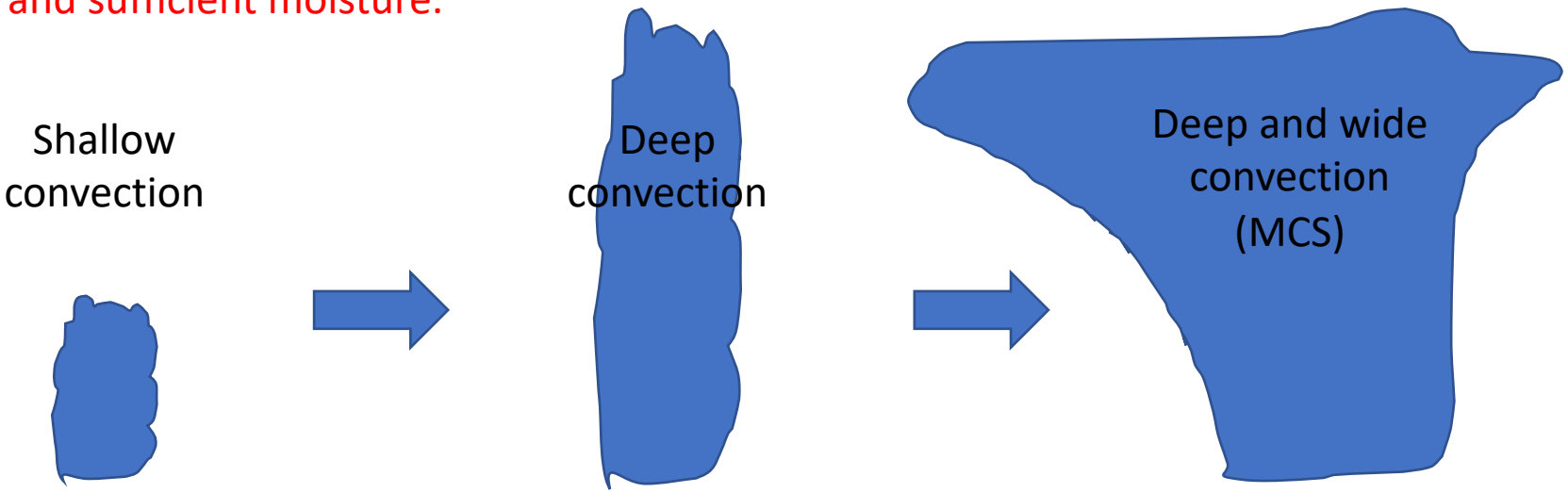

Where do they occur?

Yuan and Houze (2010)

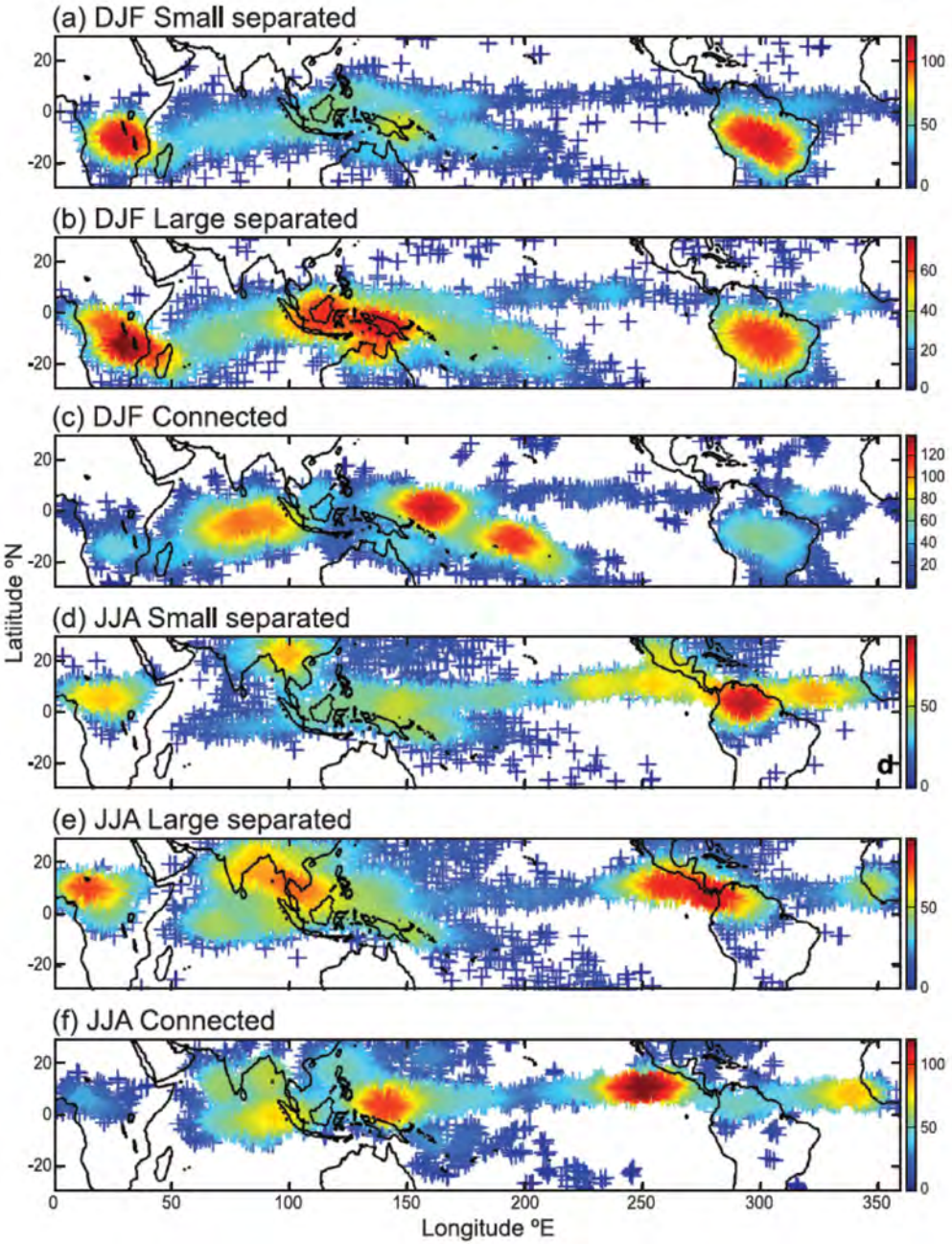

FIG. 9. Spatial distribution of active MCSs. Color of each point shows the number of active MCSs found within a circular area with radius of 5° centered on that point. (a) Small separated MCSs (<12 000 km^2; i.e., the smallest 25%) in DJF, (b) large separated MCS (>40 000 km^2; i.e., the largest 25%) in DJF, (c) connected MCS in DJF, (d)–(f) as in (a)–(c), but for JJA.

Convective precipitation is associated with intense upward and downward motion over a small horizontal area.

Stratiform precipitation usually occurs over broader regions, but is weaker.

Anvil/cirrus clouds can expand laterally far from the precipitation portion of the MCS and impact radiative heating/cooling.

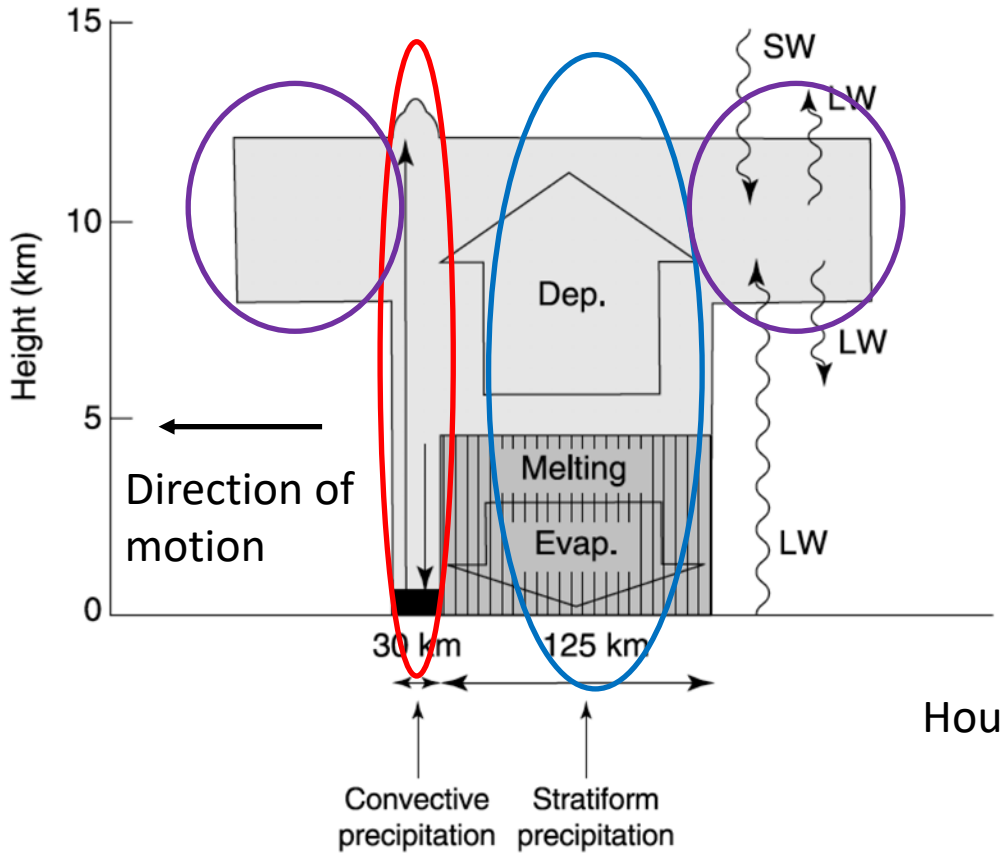

Houze (1982)

Powell et al. (2012)

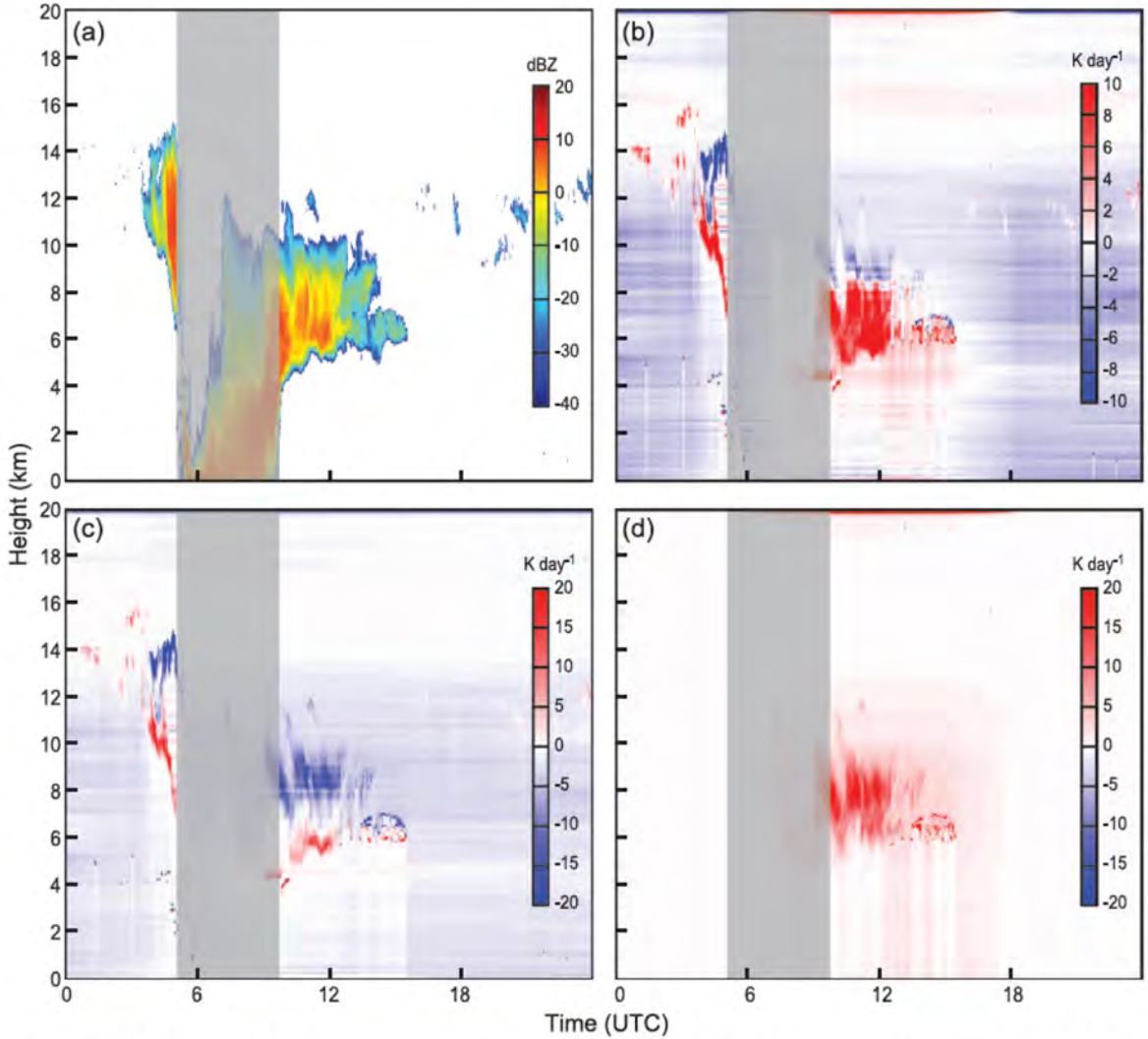

FIG. 2. (a) WACR reflectivity (dBZ) observed during the passage of an MCS over Niamey on 19 Jul 2006. (b) Heating rates (shortwave plus longwave; K day^{-1}) computed by a radiative transfer code after passing reflectivity data through a cloud retrieval. (c) As in (b), but for longwave radiation only. (d) As in (b), but for shortwave radiation only. Gray areas in each panel represent times during which WACR was partially attenuated by precipitation.

Convective and stratiform latent heating profiles take the form of first and second baroclinic modes of heating in the tropical atmosphere.

Shallow convection is similar to the negative signed second baroclinic mode, and a clear-air radiative cooling is analogous to the negative signed first baroclinic mode.

This will be important in our discussion of equatorial wave dynamics.

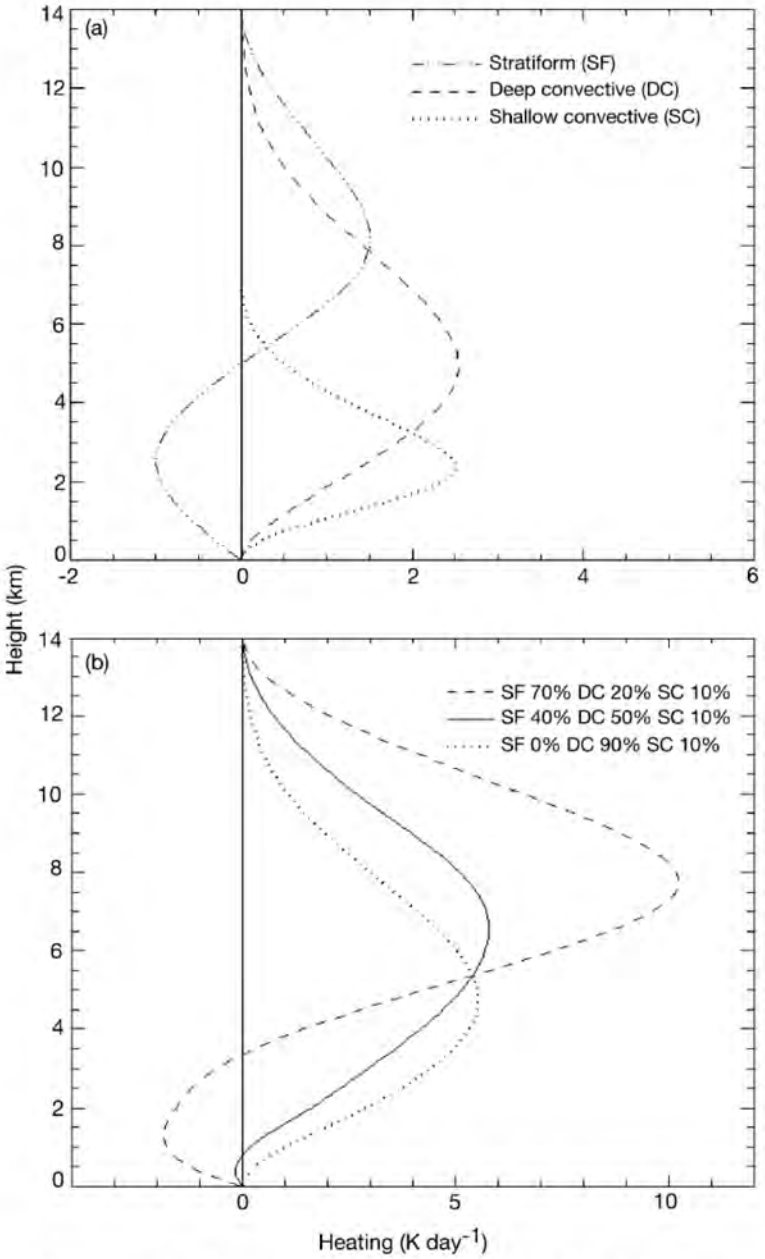

FIG. 3. Idealized stratiform, deep convective, and shallow convective latent heating profiles. The x axis is meant to be nondimensional until a precipitation amount is specified. (b) Total latent heating profiles for 0%, 40%, and 70% stratiform rain fractions, assuming 3.5 m yr^{-1} rain accumulation.

Schumacher et al. (2004)

Real (or in the case of the below figure, modeled) heating rates are more complicated.

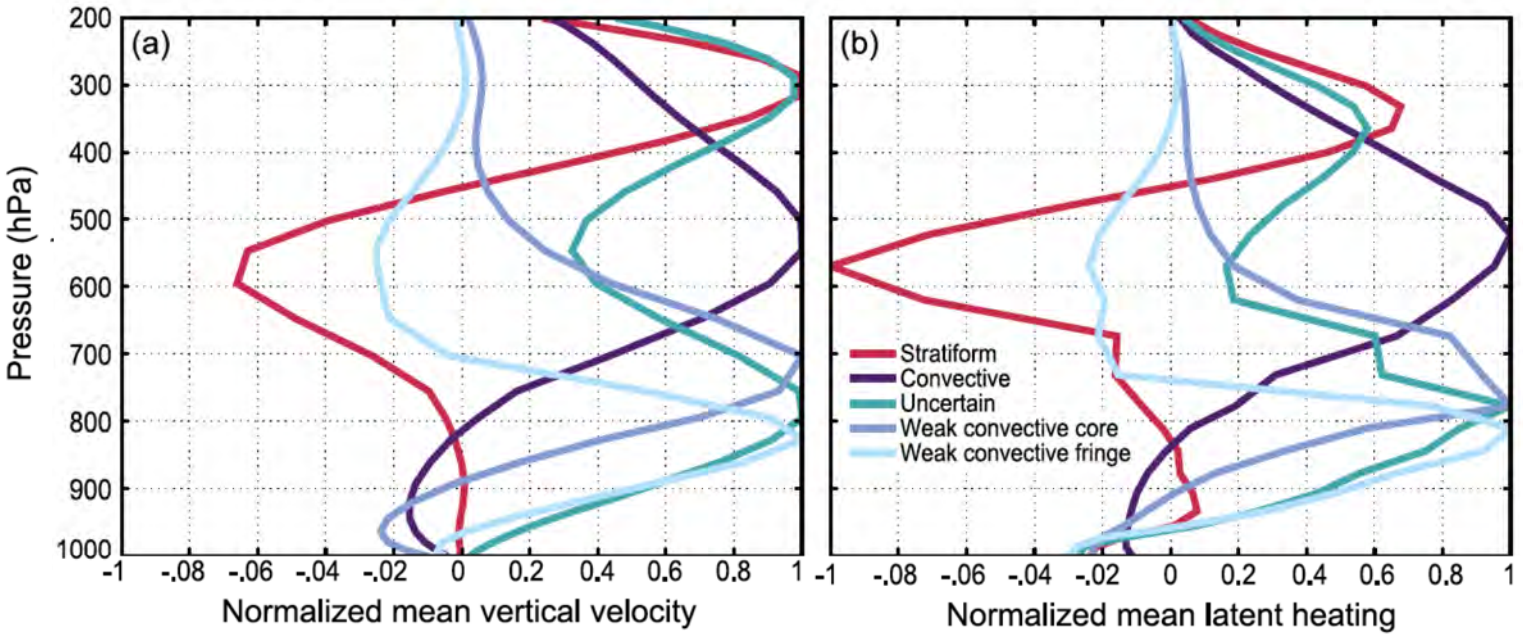

Powell et al (2016)

What are **barotropic** and **baroclinic** modes?

They are related to modes in a shallow water model.

Barotropic mode = external mode = zeroth mode: vertically averaged component. Density is only function of pressure.

Baroclinic mode = internal modes: Density is also function of temperature, salinity.

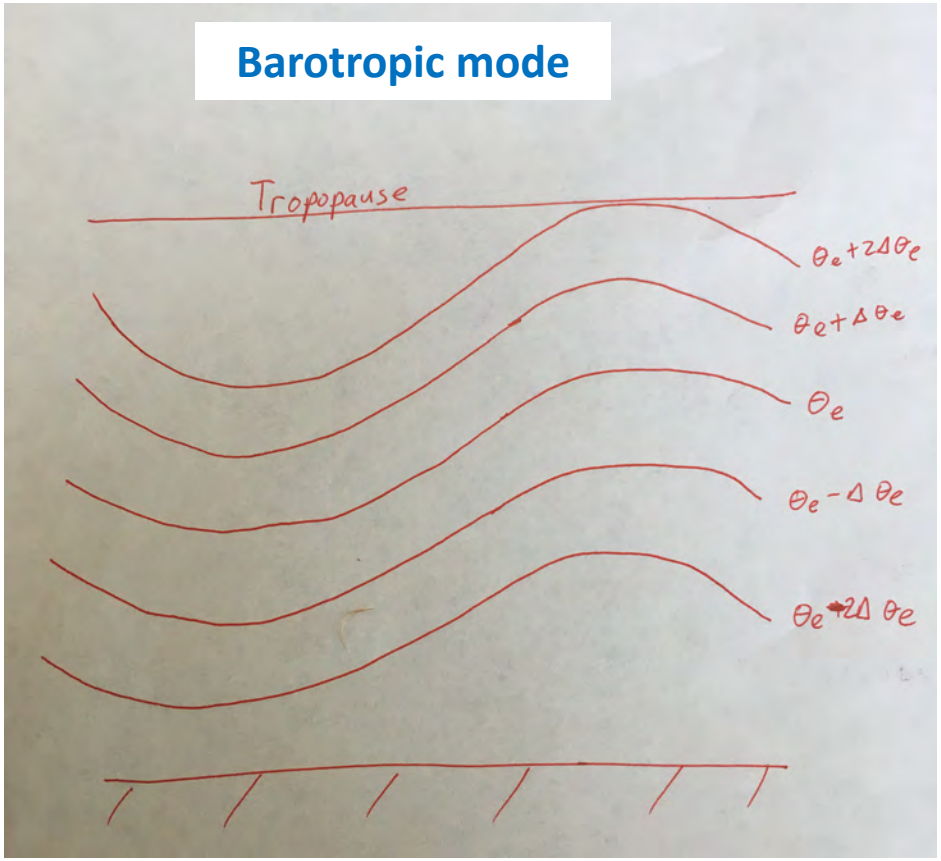

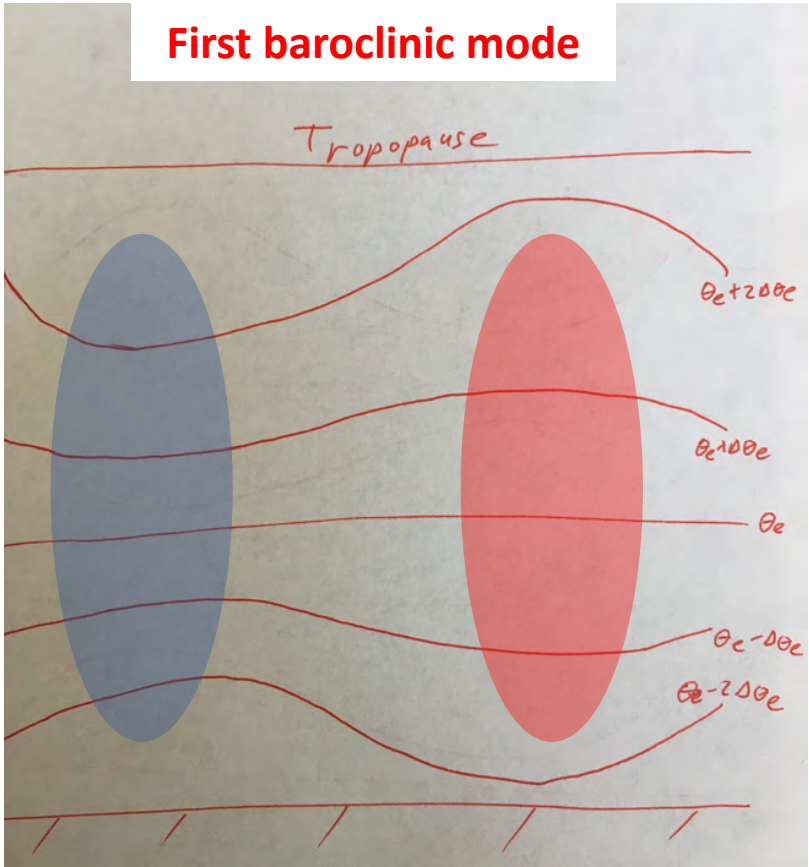

Looks like convective heating profile

Looks like stratiform or shallow convection heating profile

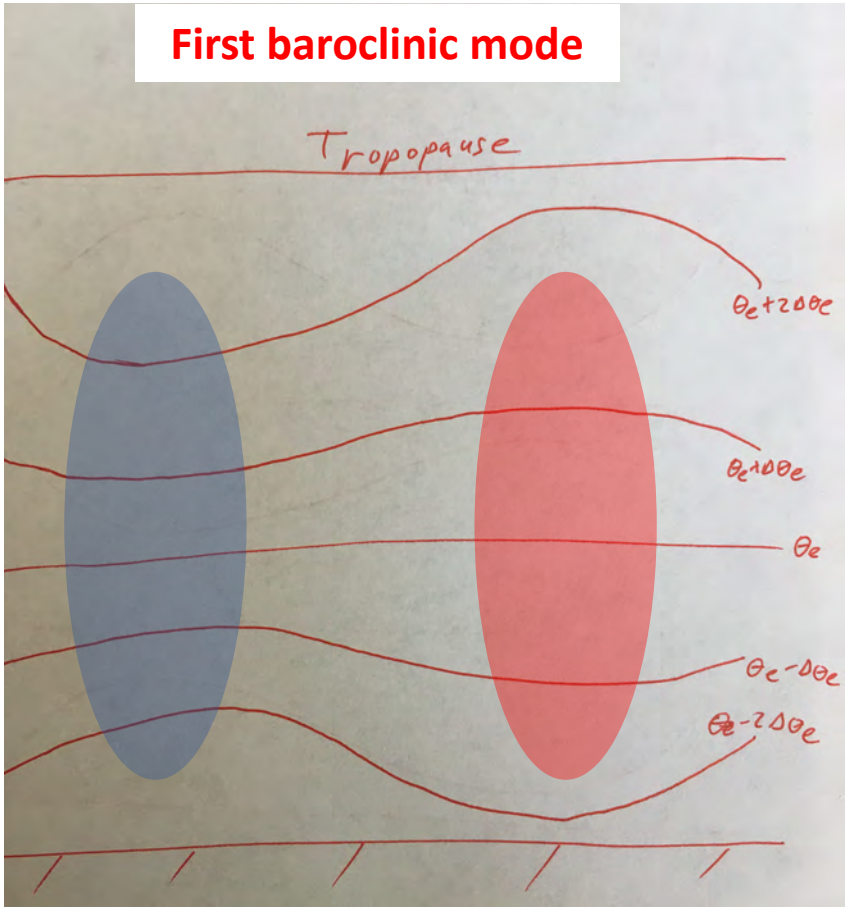

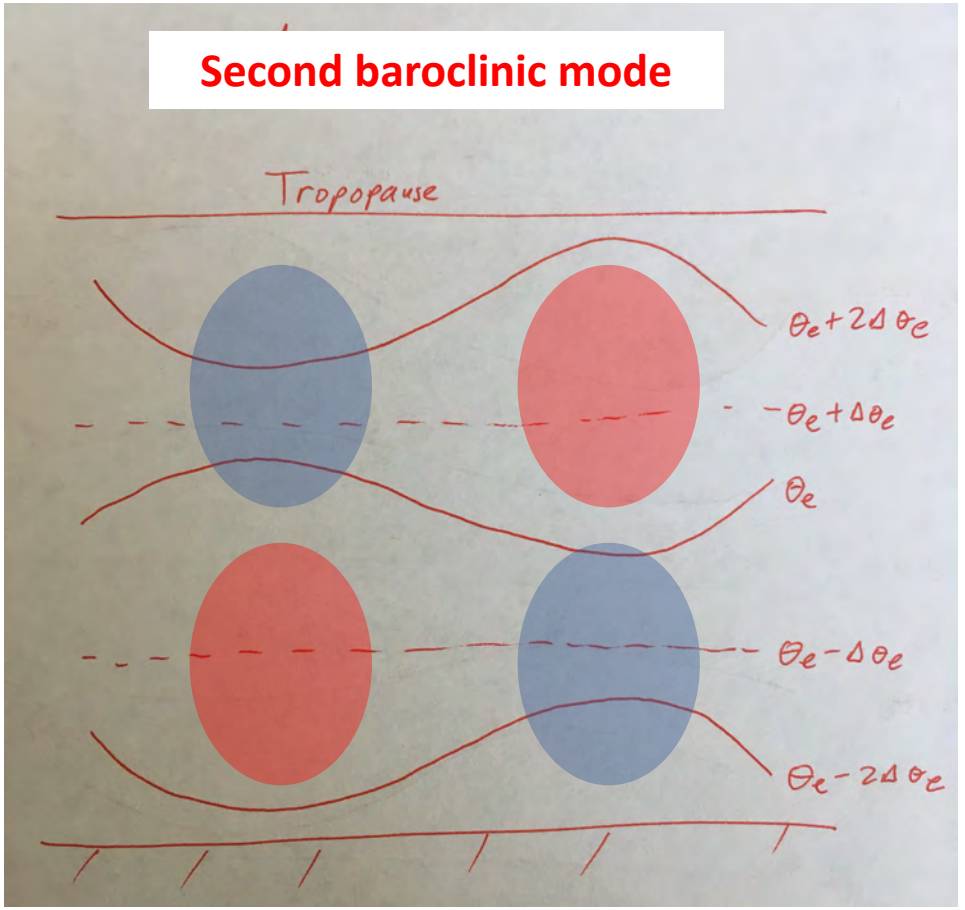

In visible satellite imagery, separating deep convection from neighboring stratiform in which it is embedded can be difficult.

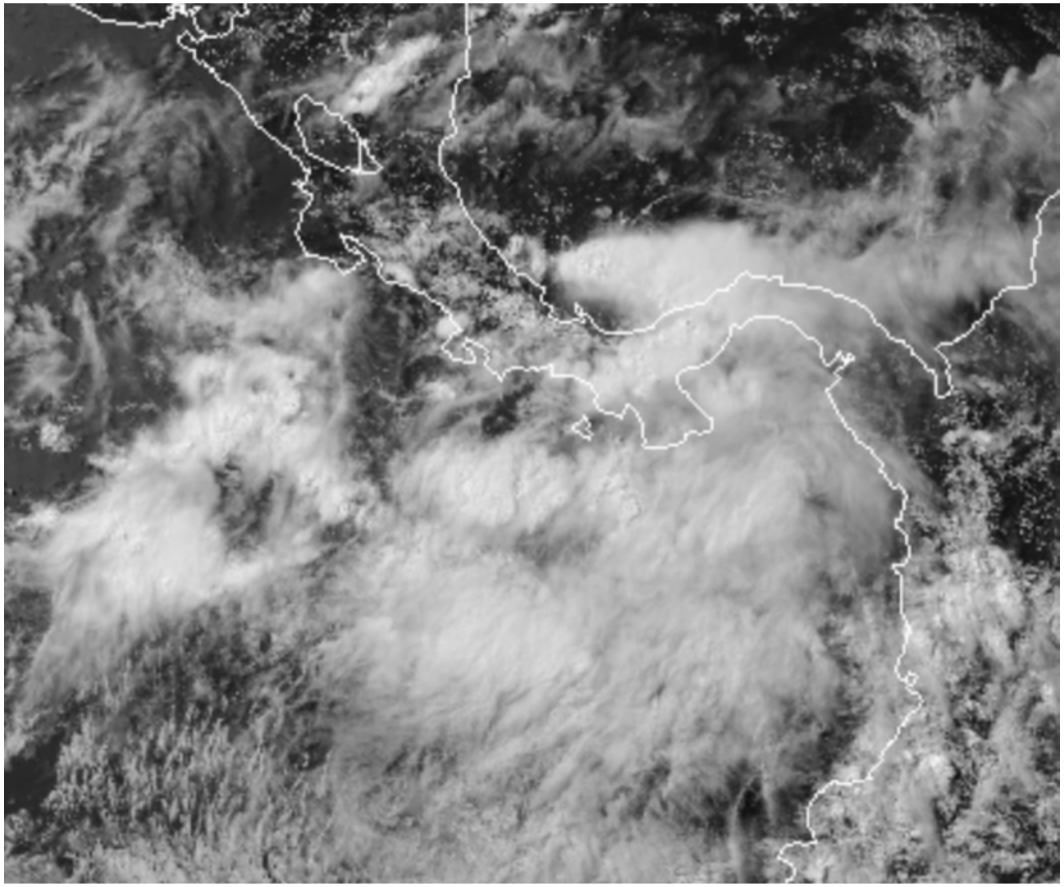

However, IR imagery can locate the highest and/or deepest clouds.

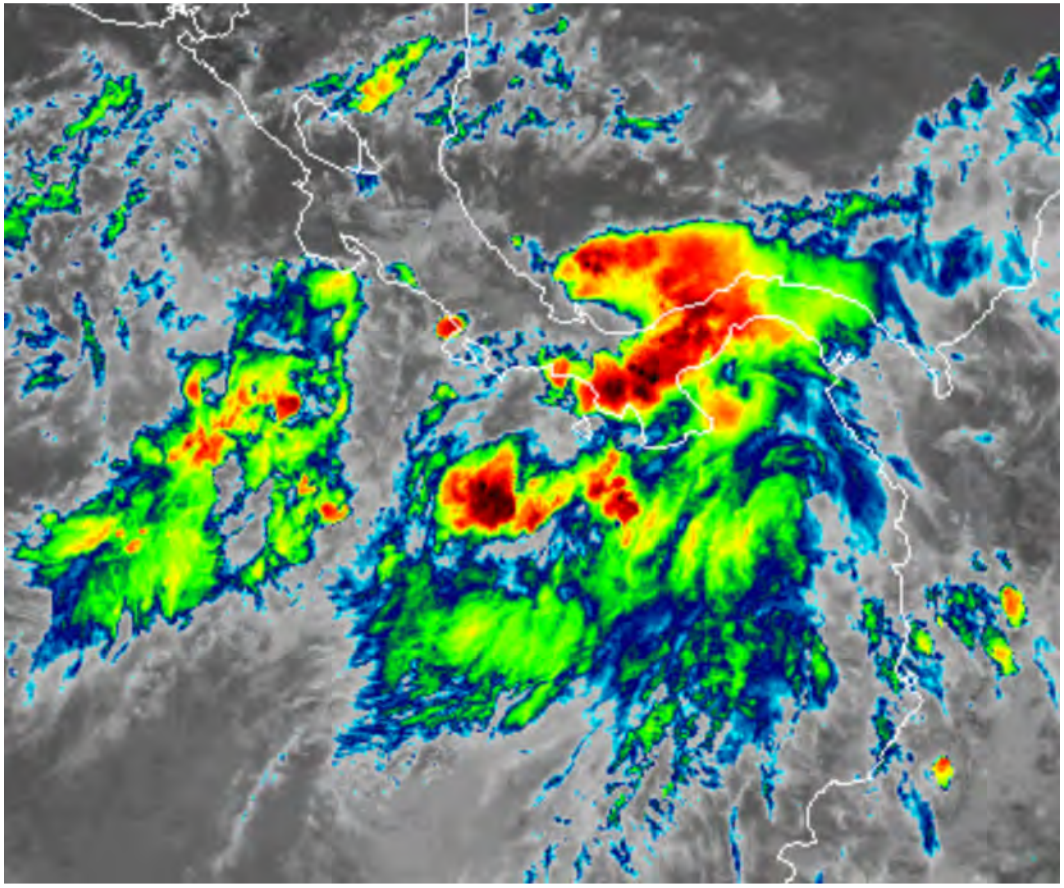

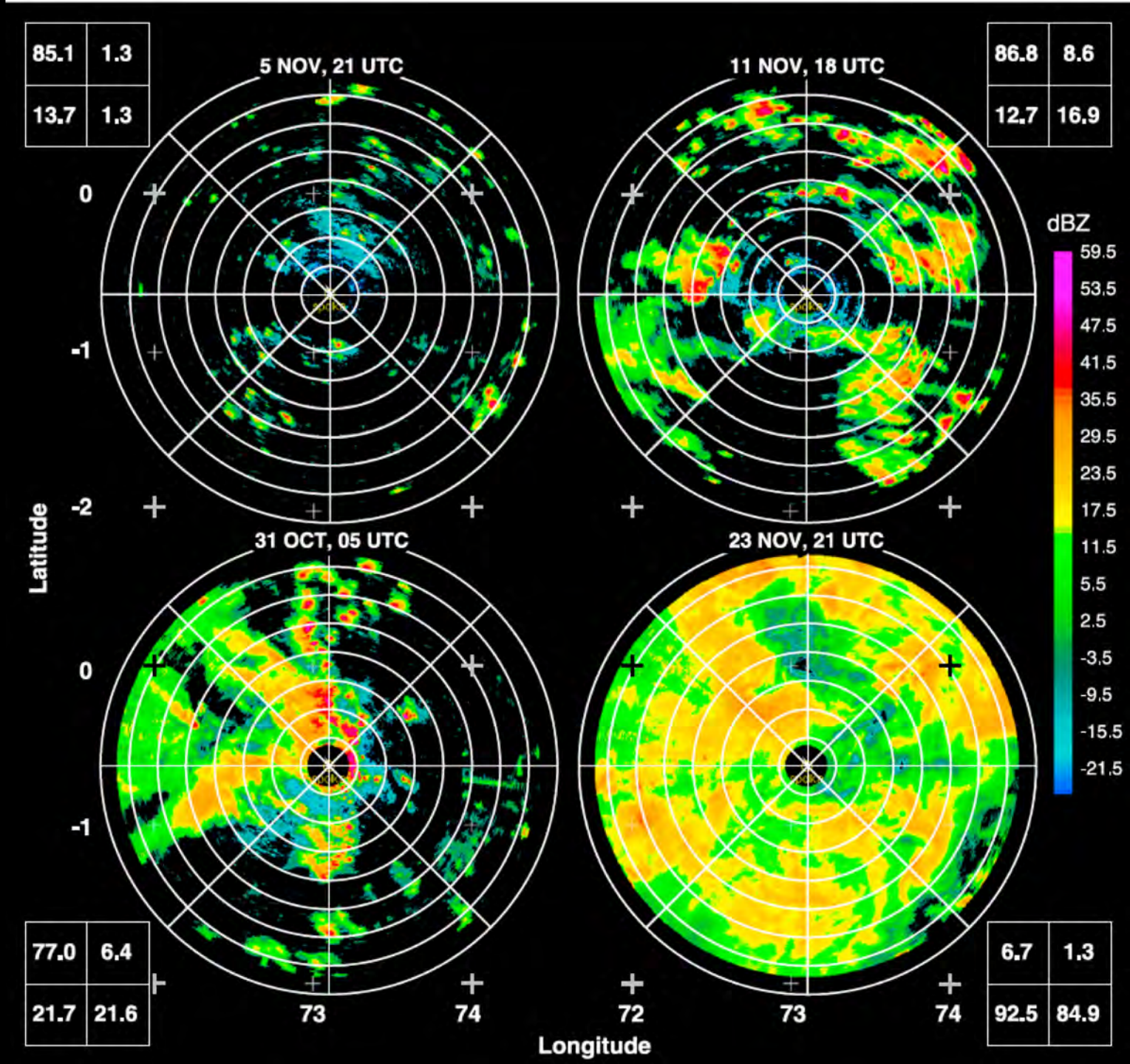
85.1
1.3
13.7
1.3
5 NOV, 21 UTC
86.8
8.6
12.7
16.9
11 NOV, 18 UTC
dBZ
59.5
53.5
47.5
41.5
35.5
29.5
23.5
17.5
11.5
5.5
2.5
-3.5
-9.5
-15.5
-21.5
0
-1
-2
Latitude
31 OCT, 05 UTC
23 NOV, 21 UTC
0
-1
77.0
6.4
21.7
21.6
6.7
1.3
92.5
84.9
73
74
72
73
74
Longitude

Zuluaga and Houze (2013)

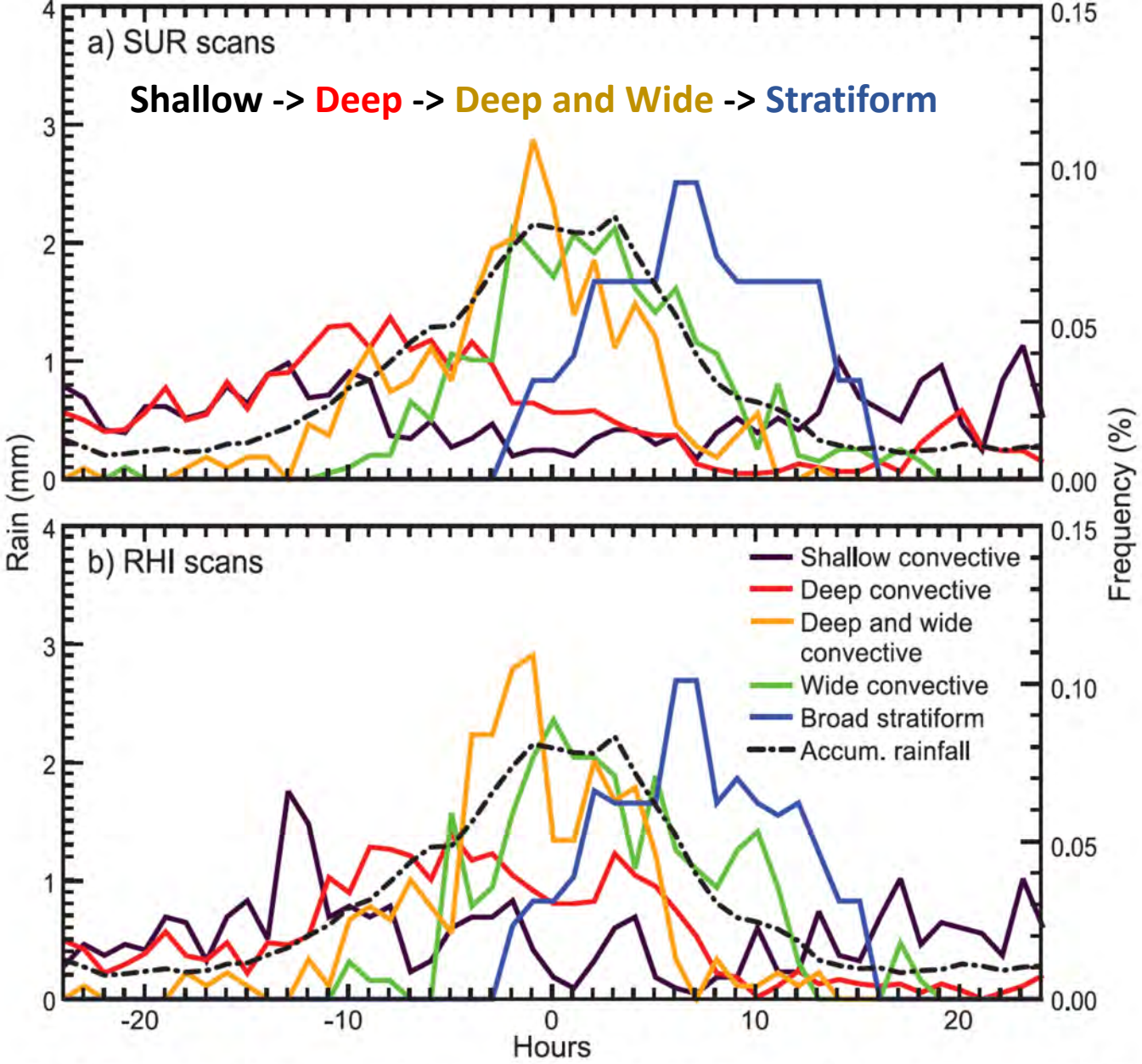

FIG. 3. Composites of the frequency of occurrence of each of the different types of radar echo structure defined in section 2 during 24 h before (negative time) and after (positive time) the composite maximum in rain accumulation (dash–dotted curve) calculated with (a) SUR and (b) RHI scanning strategy data. The right *y* axis is for the colored curves. The rainfall accumulation composite is computed by centering each of the 11 rain episodes in Fig. 2 on the time of the maximum of its running-mean curve in Fig. 2.

Zuluaga and Houze (2013)

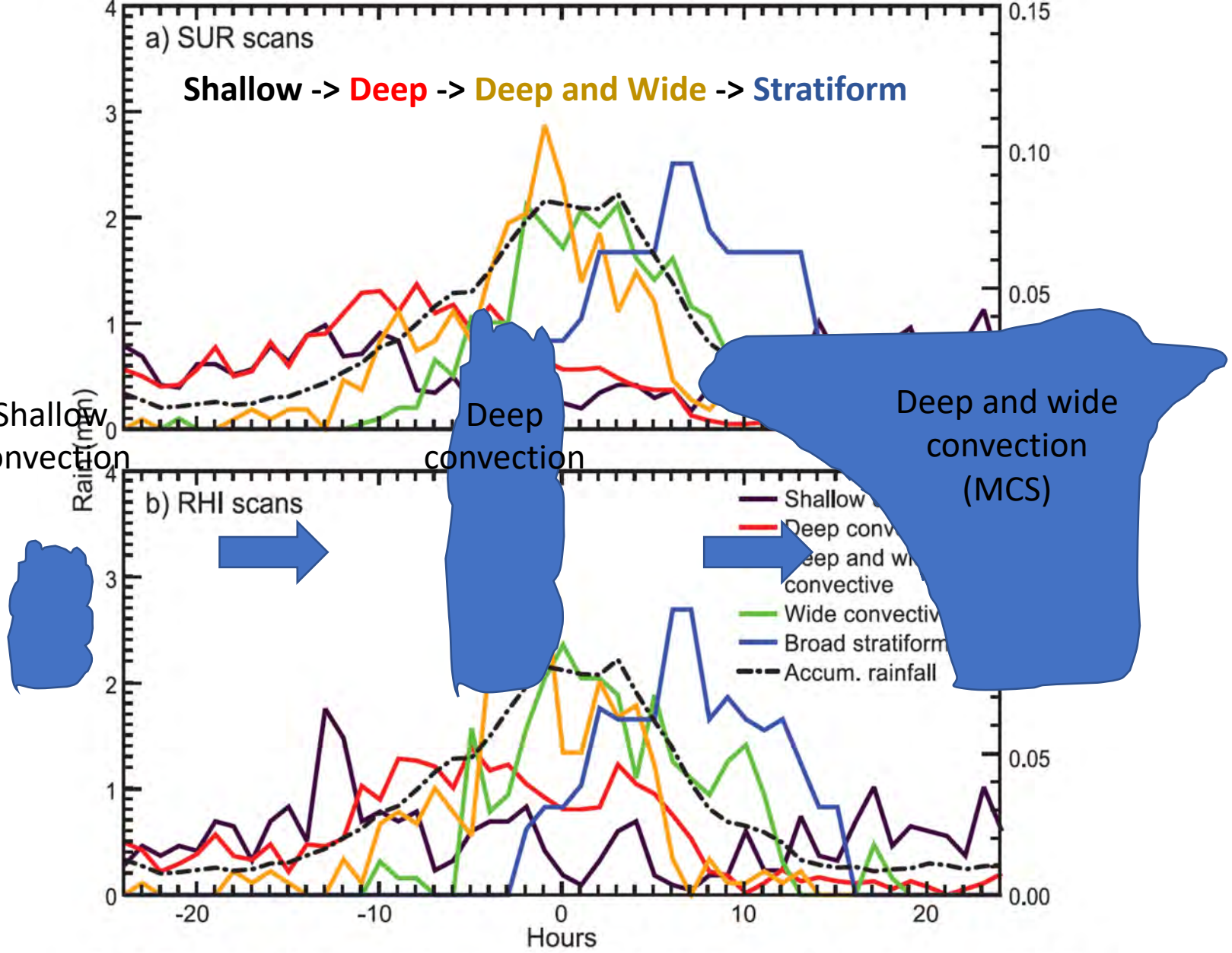

FIG. 3. Composites of the frequency of occurrence of each of the different types of radar echo structure defined in section 2 during 24 h before (negative time) and after (positive time) the composite maximum in rain accumulation (dash–dotted curve) calculated with (a) SUR and (b) RHI scanning strategy data. The right *y* axis is for the colored curves. The rainfall accumulation composite is computed by centering each of the 11 rain episodes in Fig. 2 on the time of the maximum of its running-mean curve in Fig. 2.

Powell and
Houze (2013)

Convective elements lead stratiform on multiple time scales—from diurnal variability up to sub-seasonal variability.

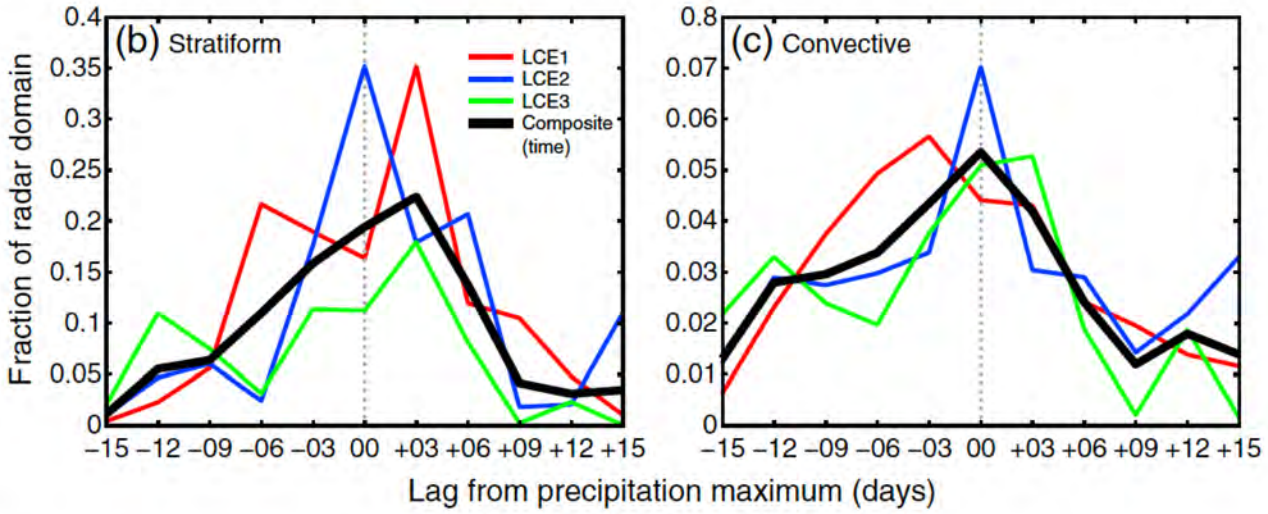

Figure 4. (a) Mean fraction of radar domain occupied by either stratiform or convective precipitating echoes during each phase of the MJO as described by WH. (b) Same as Figure 4a but composited in 3 day intervals relative to Day 0 instead of by WH MJO phase for stratiform echoes during each LCE and composited among the three LCEs. (c) Same as Figure 4b but for convective echoes.

MR3252: Tropical Meteorology

MCS Structure

Main Topics:

- Diversity in MCS structure
- Squall lines
- Kinematic and microphysical components of MCSs

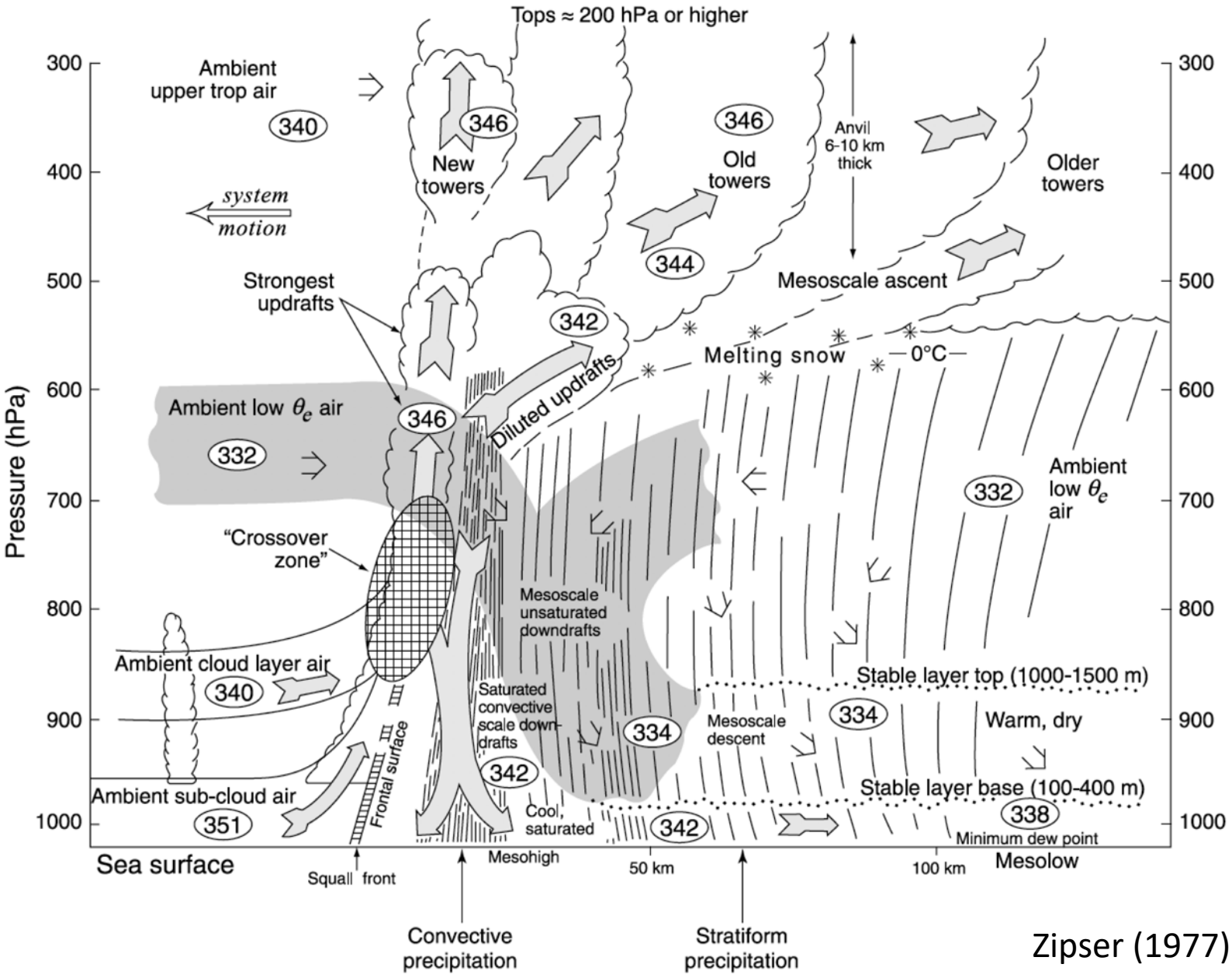
Tops ≈ 200 hPa or higher
Ambient upper trop air
340
346
New towers
346
Old towers
Anvil 6-10 km thick
Older towers
system motion
344
Mesoscale ascent
Strongest updrafts
342
Melting snow
0°C
Diluted updrafts
Ambient low θ_e air
346
332
332
Ambient low θ_e air
"Crossover zone"
Mesoscale unsaturated downdrafts
Ambient cloud layer air
340
Stable layer top (1000-1500 m)
Saturated convective scale down-drafts
334
Mesoscale descent
334
Warm, dry
342
Ambient sub-cloud air
351
Frontal surface
Cool, saturated
342
Stable layer base (100-400 m)
338
Minimum dew point
Pressure (hPa)
300
400
500
600
700
800
900
1000
Sea surface
Squall front
Mesohigh
50 km
100 km
Mesolow
Convective precipitation
Stratiform precipitation

Zipser (1977)

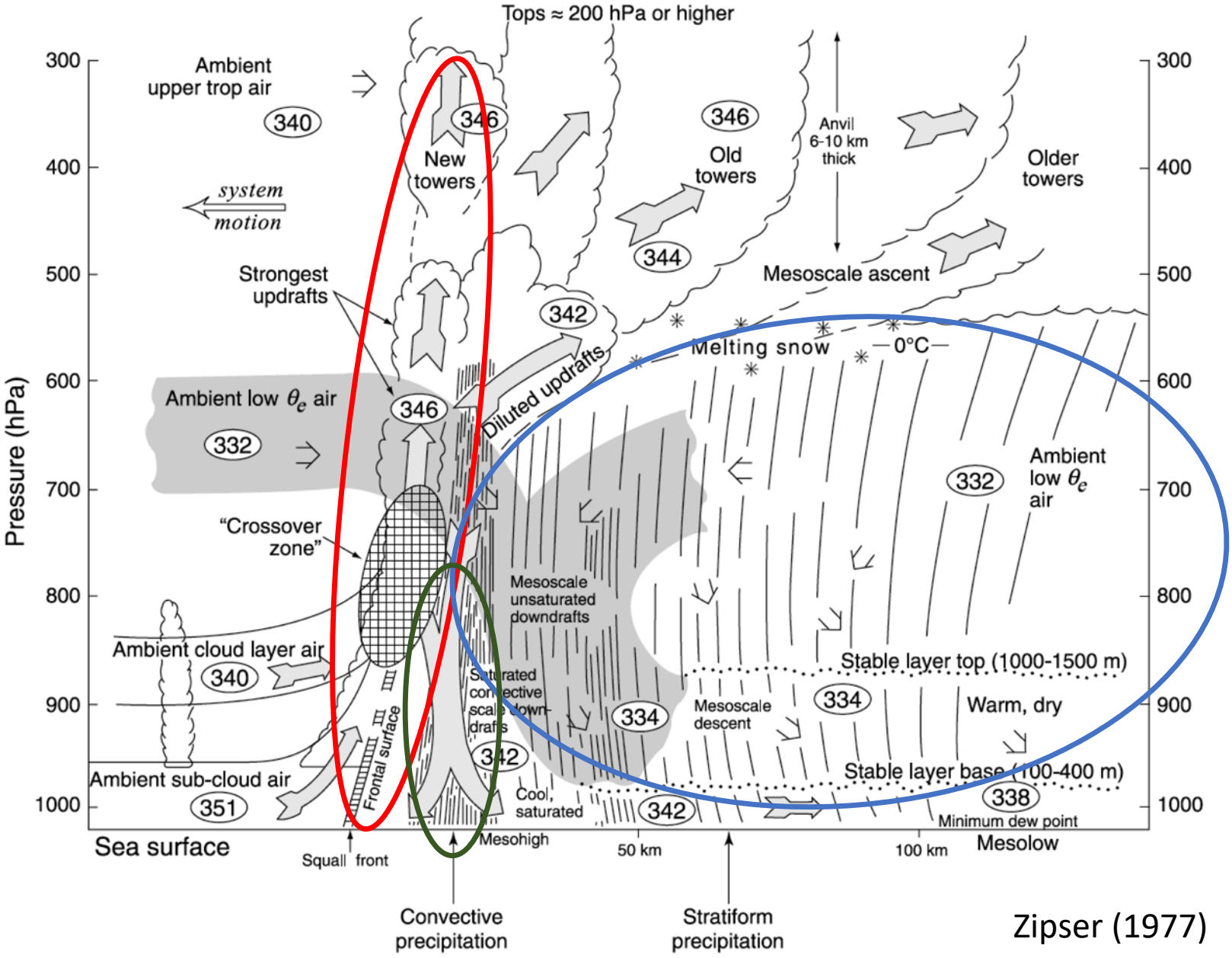
Tops ≈ 200 hPa or higher
Ambient upper trop air
340
346
New towers
346
Old towers
Anvil 6-10 km thick
Older towers
system motion
344
Mesoscale ascent
Strongest updrafts
342
Melting snow
0°C
Diluted updrafts
Ambient low θ_e air
346
332
332
Ambient low θ_e air
"Crossover zone"
Mesoscale unsaturated downdrafts
Ambient cloud layer air
340
Stable layer top (1000-1500 m)
Saturated convective scale downdrafts
334
Mesoscale descent
334
Warm, dry
342
Stable layer base (100-400 m)
Ambient sub-cloud air
351
Frontal surface
Cool, saturated
342
338
Minimum dew point
Sea surface
Squall front
Mesohigh
50 km
100 km
Mesolow
Pressure (hPa)
300
400
500
600
700
800
900
1000
Convective precipitation
Stratiform precipitation

Zipser (1977)

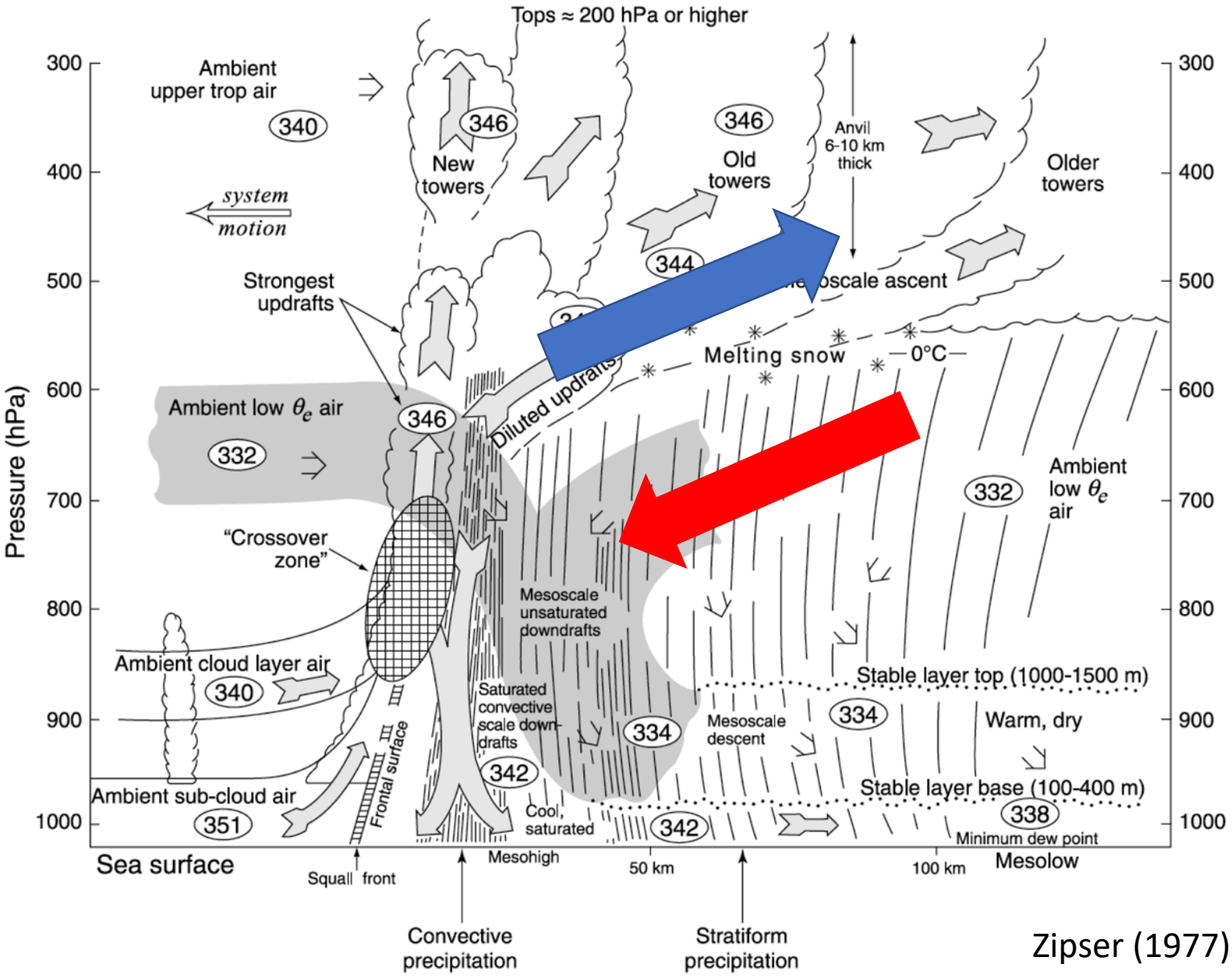
Tops ≈ 200 hPa or higher
Ambient upper trop air
340
346
New towers
346
Old towers
Anvil 6-10 km thick
Older towers
system motion
Strongest updrafts
344
Mesoscale ascent
Melting snow
0°C
Diluted updrafts
Ambient low θ_e air
346
332
332
Ambient low θ_e air
"Crossover zone"
Mesoscale unsaturated downdrafts
Ambient cloud layer air
340
Saturated convective scale down-drafts
334
Mesoscale descent
334
Stable layer top (1000-1500 m)
Warm, dry
342
Ambient sub-cloud air
351
Frontal surface
Cool, saturated
342
Stable layer base (100-400 m)
338
Minimum dew point
Pressure (hPa)
300
400
500
600
700
800
900
1000
Sea surface
Squall front
Mesohigh
50 km
100 km
Mesolow
Convective precipitation
Stratiform precipitation

Zipser (1977)

Houze et al. (1989)

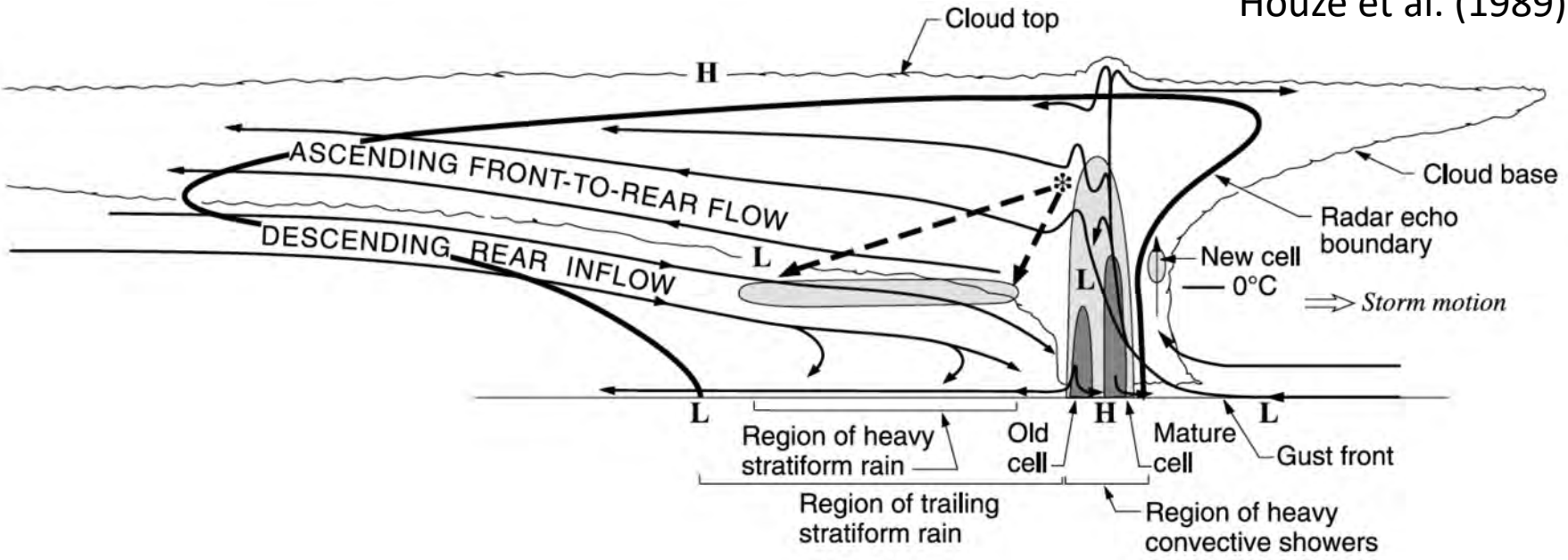

Figure 14. Conceptual model of the kinematic, microphysical, and radar echo structure of a convective line with trailing-stratiform precipitation viewed in a vertical cross section oriented perpendicular to the convective line (and generally parallel to its motion). Intermediate and strong radar reflectivity is indicated by medium and dark shading, respectively. H and L indicate centers of positive and negative pressure perturbations, respectively. Dashed-line arrows indicate fallout trajectories of ice particles passing through the melting layer. From *Houze et al.* [1989].

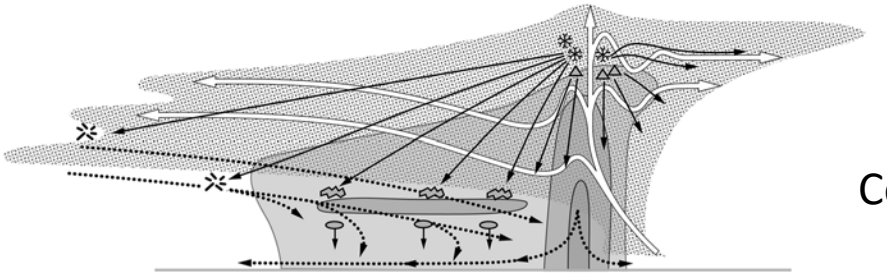

Cetrone and Houze (2011)

In visible satellite imagery, separating deep convection from neighboring stratiform in which it is embedded can be difficult.

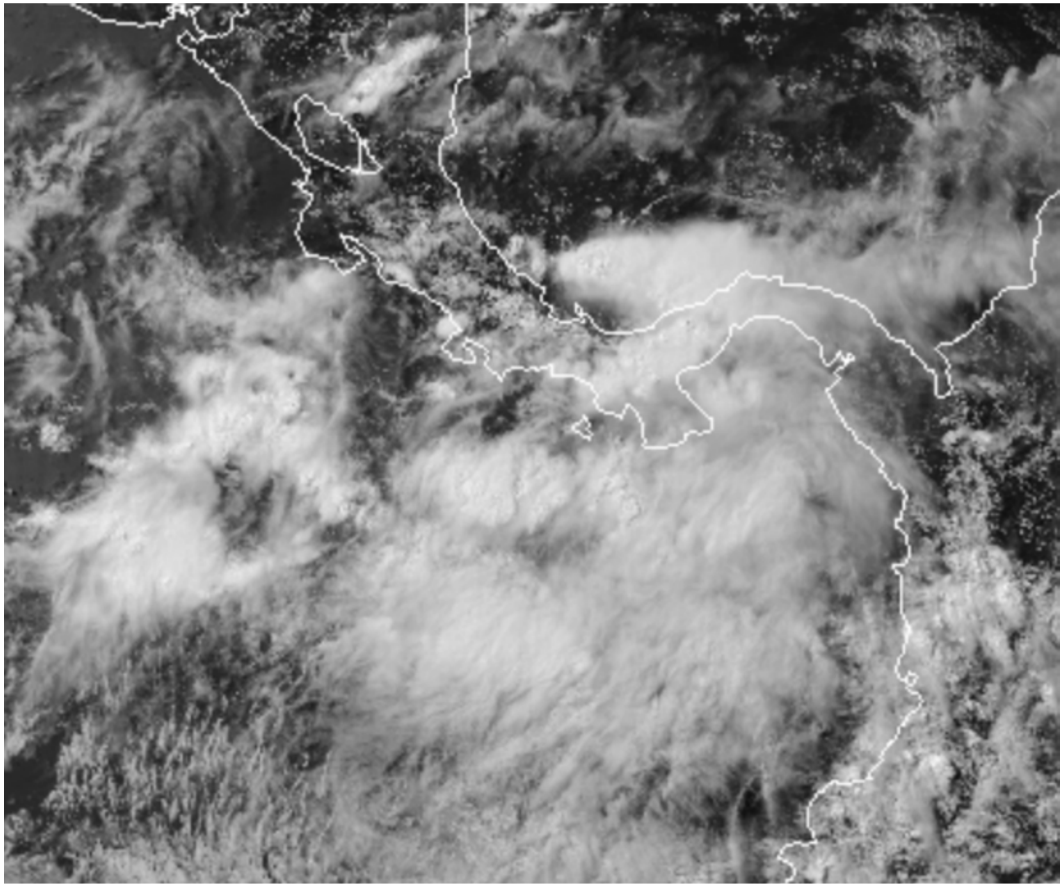

However, IR imagery can locate the highest and/or deepest clouds.

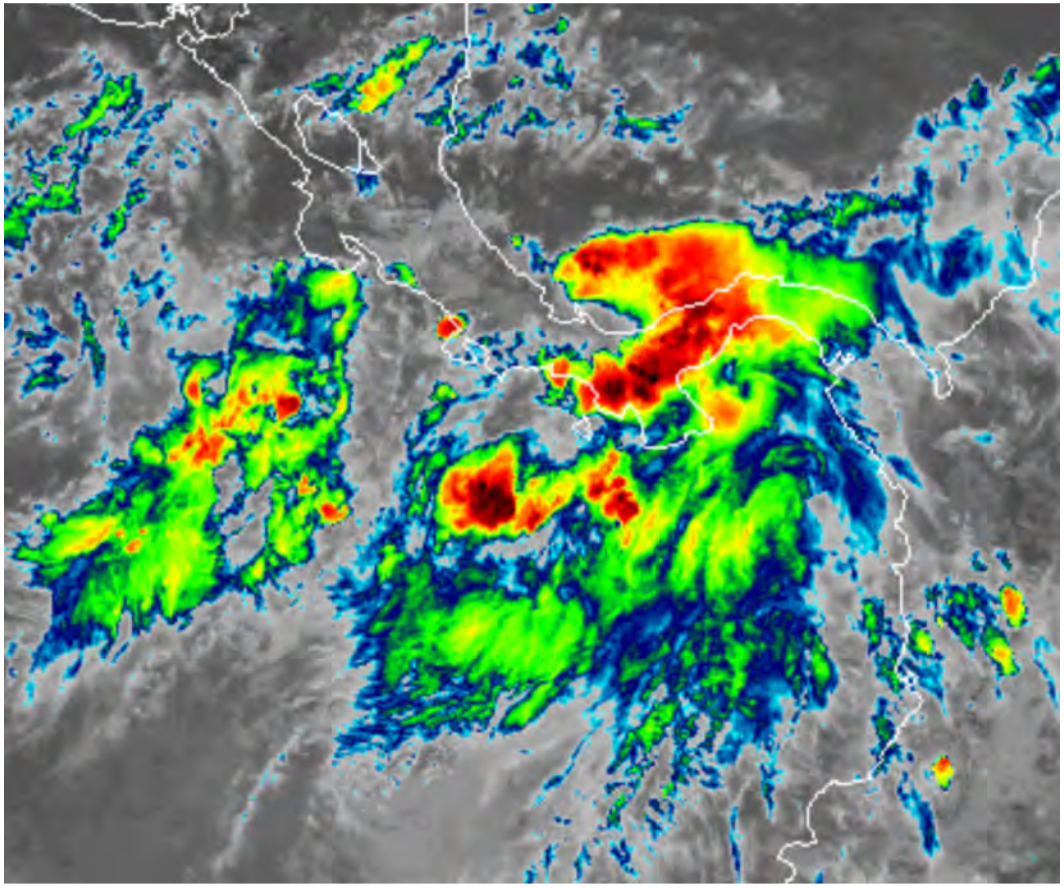

Convective and stratiform areas are also usually obvious in precipitation radar data, but anvil/cirrus clouds can only be detected using satellite imagery.

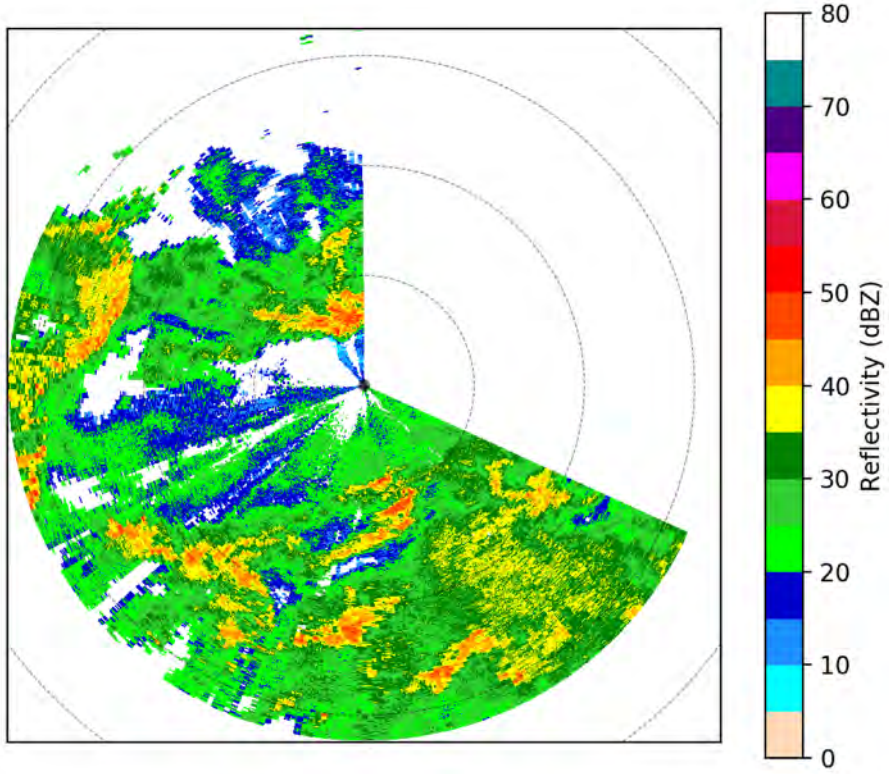

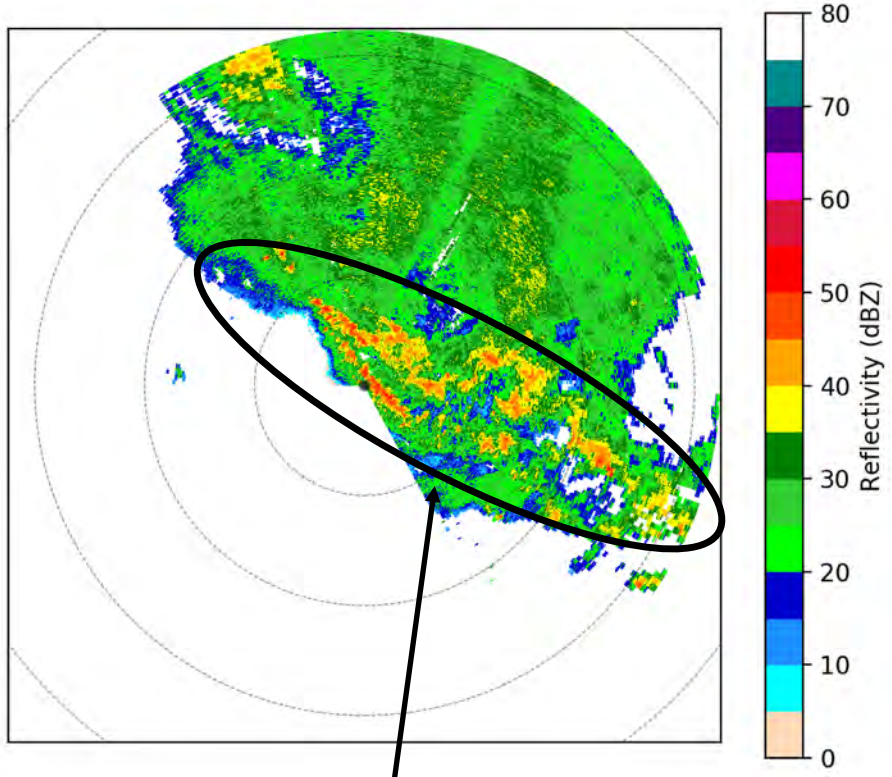

Leading convective line with trailing stratiform to the NE

MCSs do not always contain a leading convective line with trailing stratiform.
Sometimes the stratiform develops “ahead” of the convective line or parallel to it.

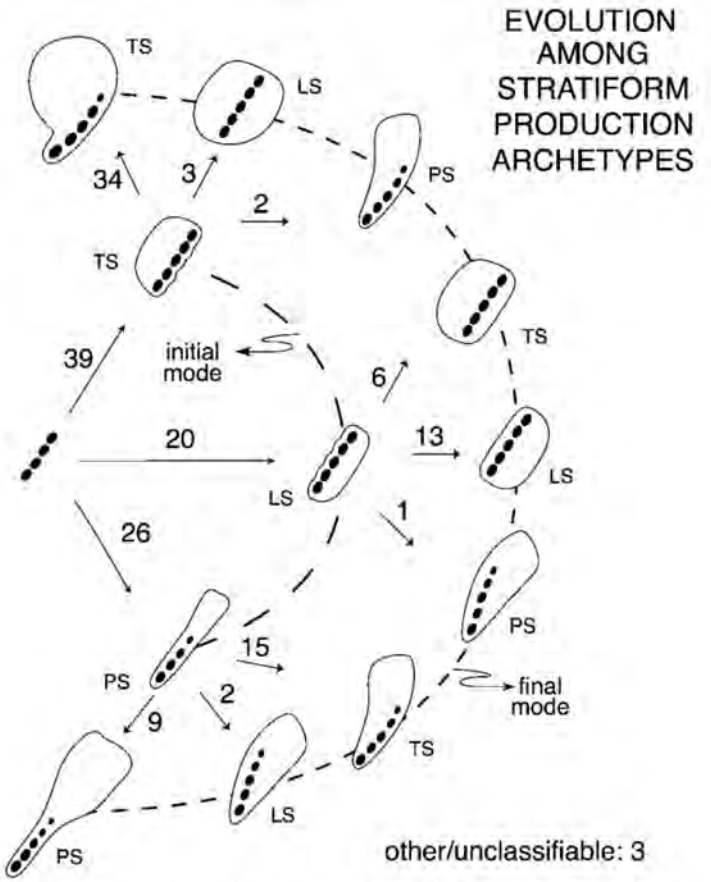

FIG. 9. Illustration of evolutionary pathways for MCSs in this study. Labels along each pathway denote the initial and final modes of stratiform precipitation production. The total number of cases following each step is indicated. Idealized composite positions of convective elements and stratiform precipitation are depicted schematically along each pathway. Note: some pairs of evolutionary pathways (e.g., TS → PS and PS → TS) resulted in generally similar reflectivity patterns. As discussed in the text, MCSs were classified based upon their predominant organizational mode, which could be either their initial or final organization.

*This study was for *mid-latitude* MCSs.

Parker and Johnson (2000)

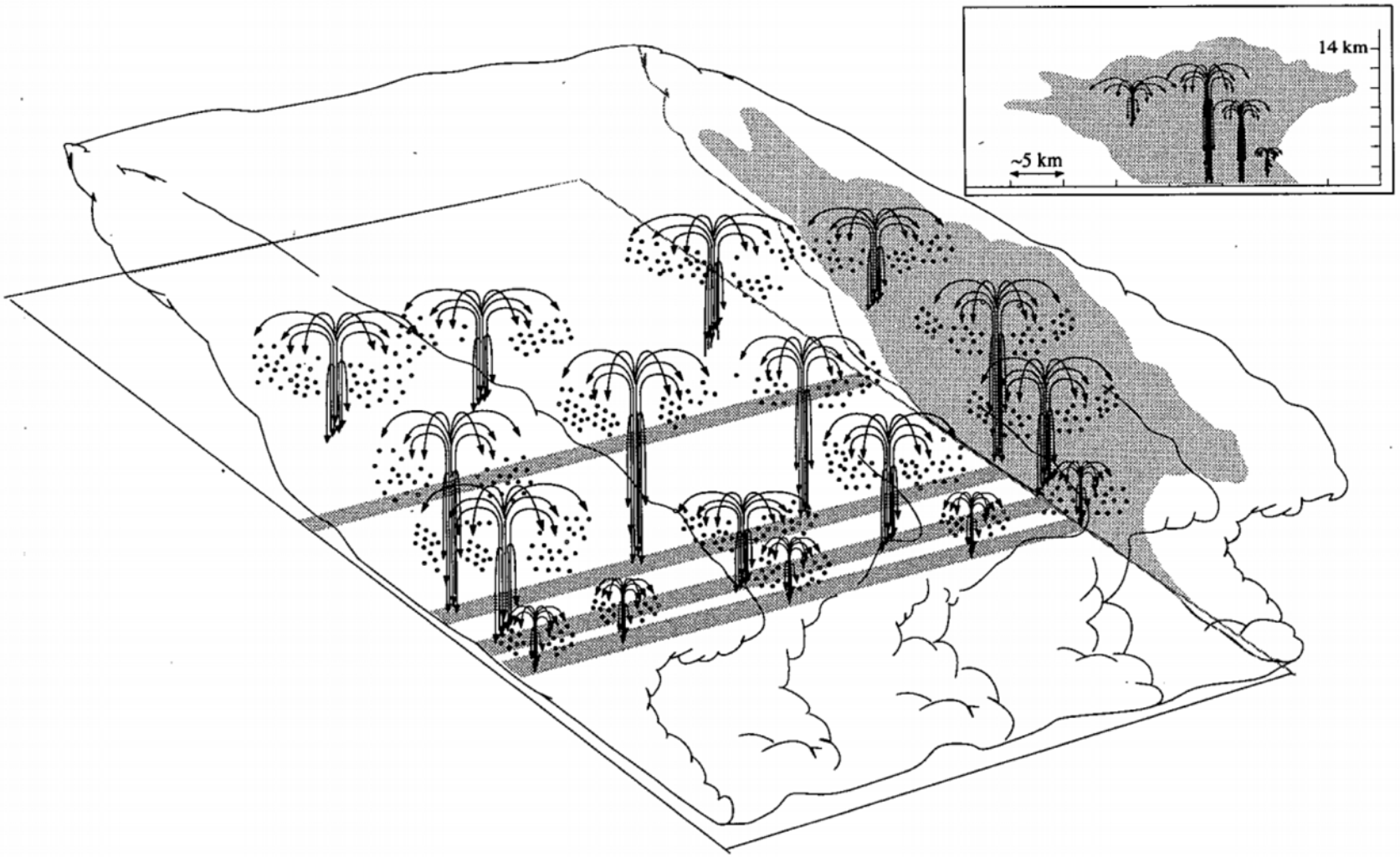

FIG. 15. Conceptual model of an ensemble of particle fountains in a multicellular storm in perspective view. Shaded area represents radar reflectivity echo along a cross section perpendicular to the line of storms. Cloud boundary indicated by scalloped outline. Inset shows approximate scales and arrangement of largest particle fountains relative to radar echo.

Yuter and Houze (1995)

Smoothed kinematic structure of leading line/trailing stratiform MCS. Radar echo shown for reference.

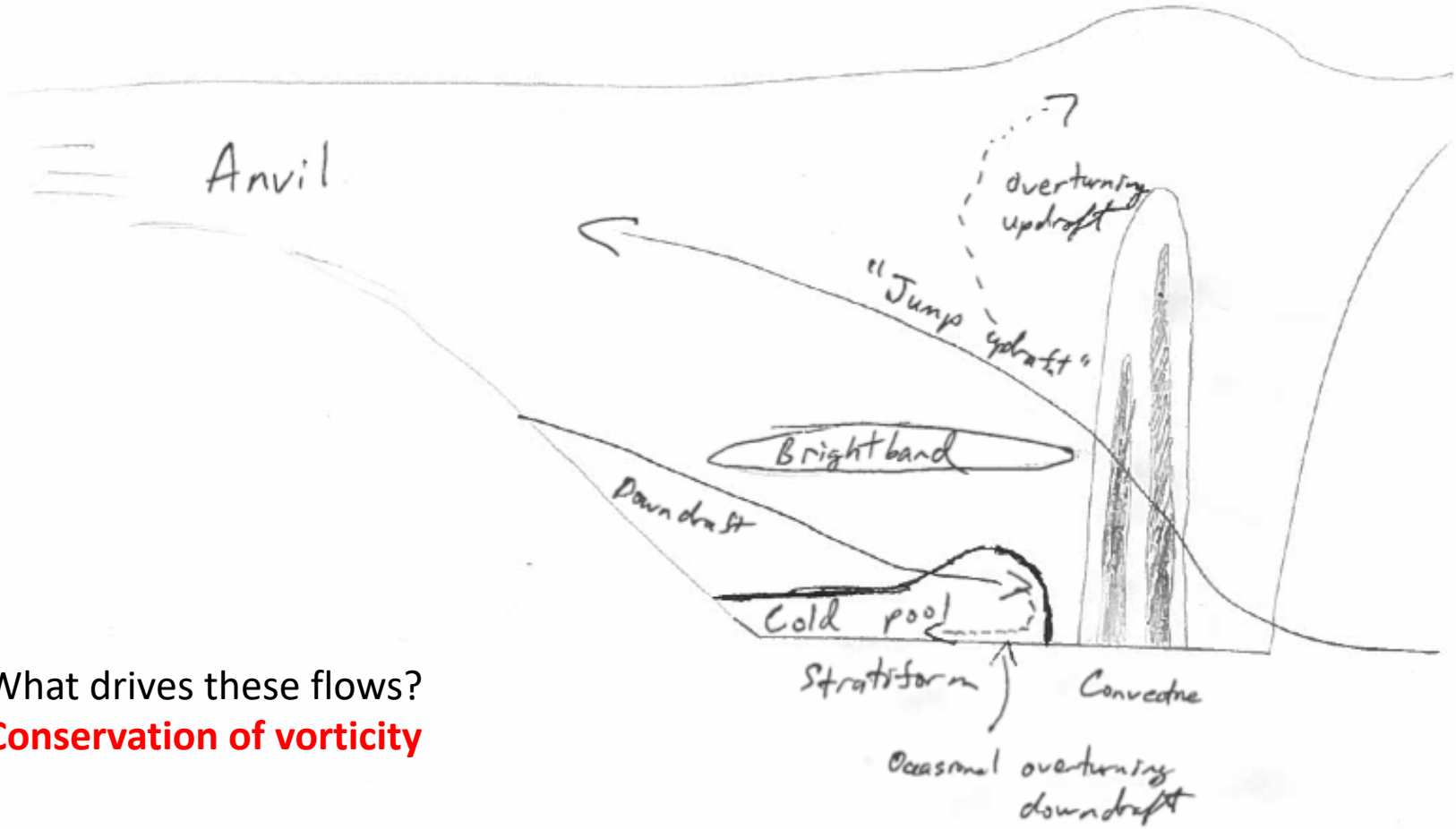

What drives these flows?

Conservation of vorticity

What drives these flows? **Conservation of vorticity**

Start with

$$\frac{D\xi}{Dt} + g\frac{\partial}{\partial x}\left(\frac{\theta^*}{\hat{\theta}}\right) = 0$$

2-dimensional flow with f = 0.

and define a streamfunction:

$$(u, w) = (\psi_z, -\psi_x)$$

Assume a steady state ($\partial/\partial t = 0$), and substitute the streamfunctions into the vorticity equation (2D along *u*, *w* cross-section:

$$\psi_z \frac{\partial}{\partial x}(\psi_{zz} + \psi_{xx}) - \psi_x \frac{\partial}{\partial z}(\psi_{zz} + \psi_{xx}) + g\frac{\partial}{\partial x}\left(\frac{\theta^*}{\hat{\theta}}\right) = 0$$

Then the flow is controlled by the large-scale environment and the horizontal gradient of buoyancy.

Zonal wind

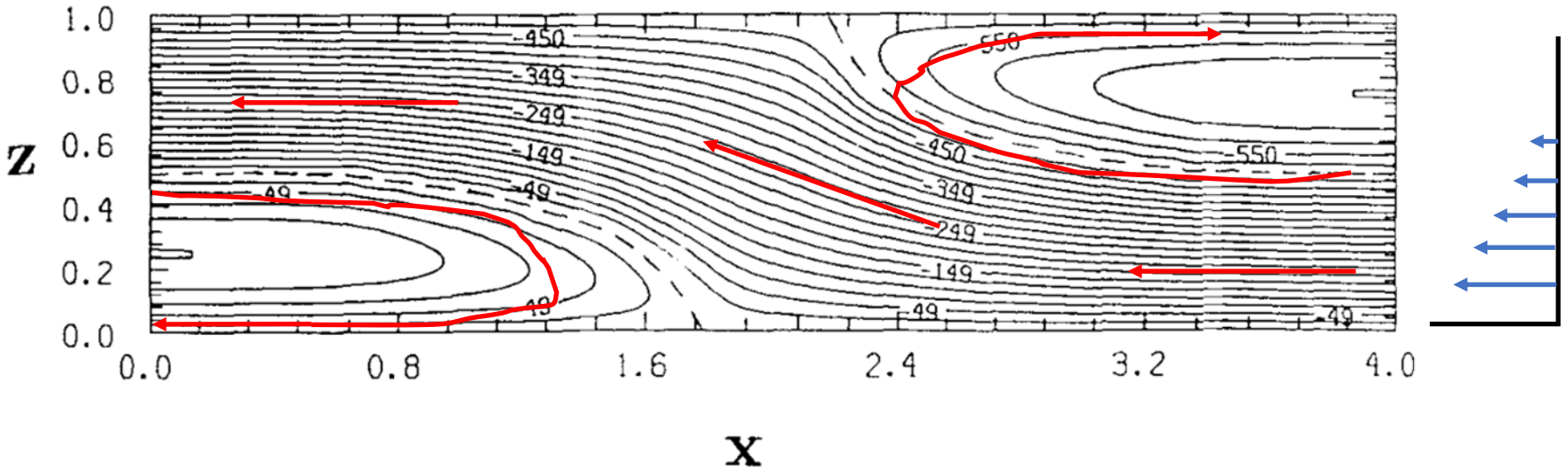

Figure 4. Two-dimensional relative streamfunction, ψ, for the stationary free-boundary solution for $h = h_0 = \frac{1}{2}$. The approximate positions of the free boundaries are shown by broken lines. ψ normalized by $U_0 H$ and multiplied by 100. Dynamical scale $L_m = 4$.

Also, CAPE can contribute to horizontal and vertical motions in MCSs.

Take the vertical momentum equations, neglect friction and Coriolis and multiply by **v***.

$$\mathbf{v}\cdot\left(\frac{\mathrm{D}\mathbf{v}}{\mathrm{D}t} = -\frac{1}{\rho_0}\nabla p^* + B\mathbf{k}\right)$$

Use Leibnitz's Integral Rule applied to a streamline (ψ is constant), such that:

$$w\mathcal{H} = \frac{\mathrm{D}}{\mathrm{D}t}\int_{z_{inflow}}^{z(t)} \mathcal{H}(z,t)\,dz$$

where $\mathcal{H}$ is some quantity that depends only on how far upward an inflowing parcel has risen. Outcome is the Bernoulli equation!

$$\frac{1}{2}(u^2 + w^2) + \frac{p^*}{\rho_0} - \int_{z_{inflow}}^{z(t)} g\left(\frac{\theta^*}{\hat{\theta}}\right)dz = constant$$

This states that CAPE can be converted not only to vertical motion (*w*) but also to horizontal motion (*u*) or enthalpy (p^*/ρ_0).

*See Houze (2014), Page 252 for further derivation.

Barnes and Houze (2014)

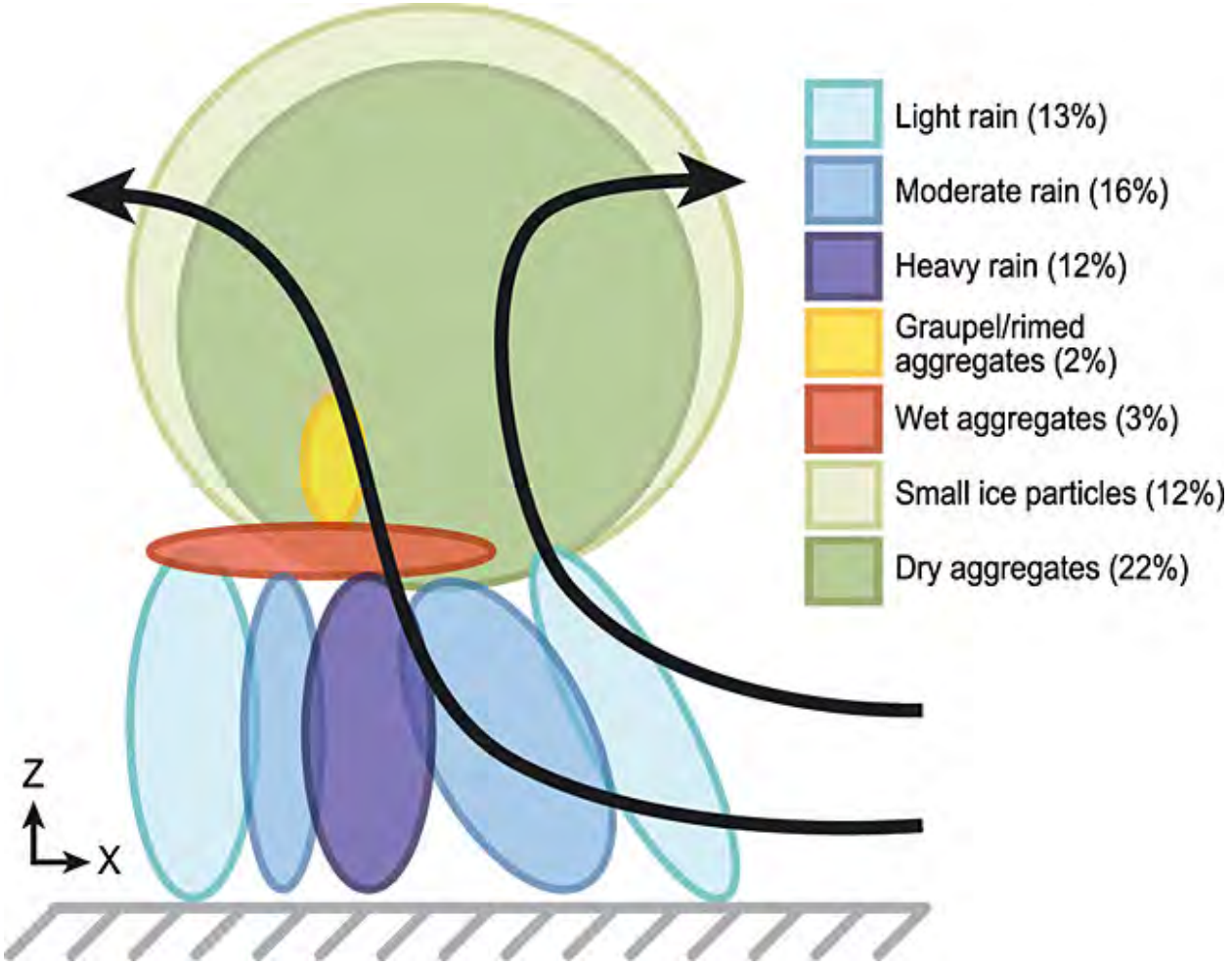

Barnes and Houze (2014)

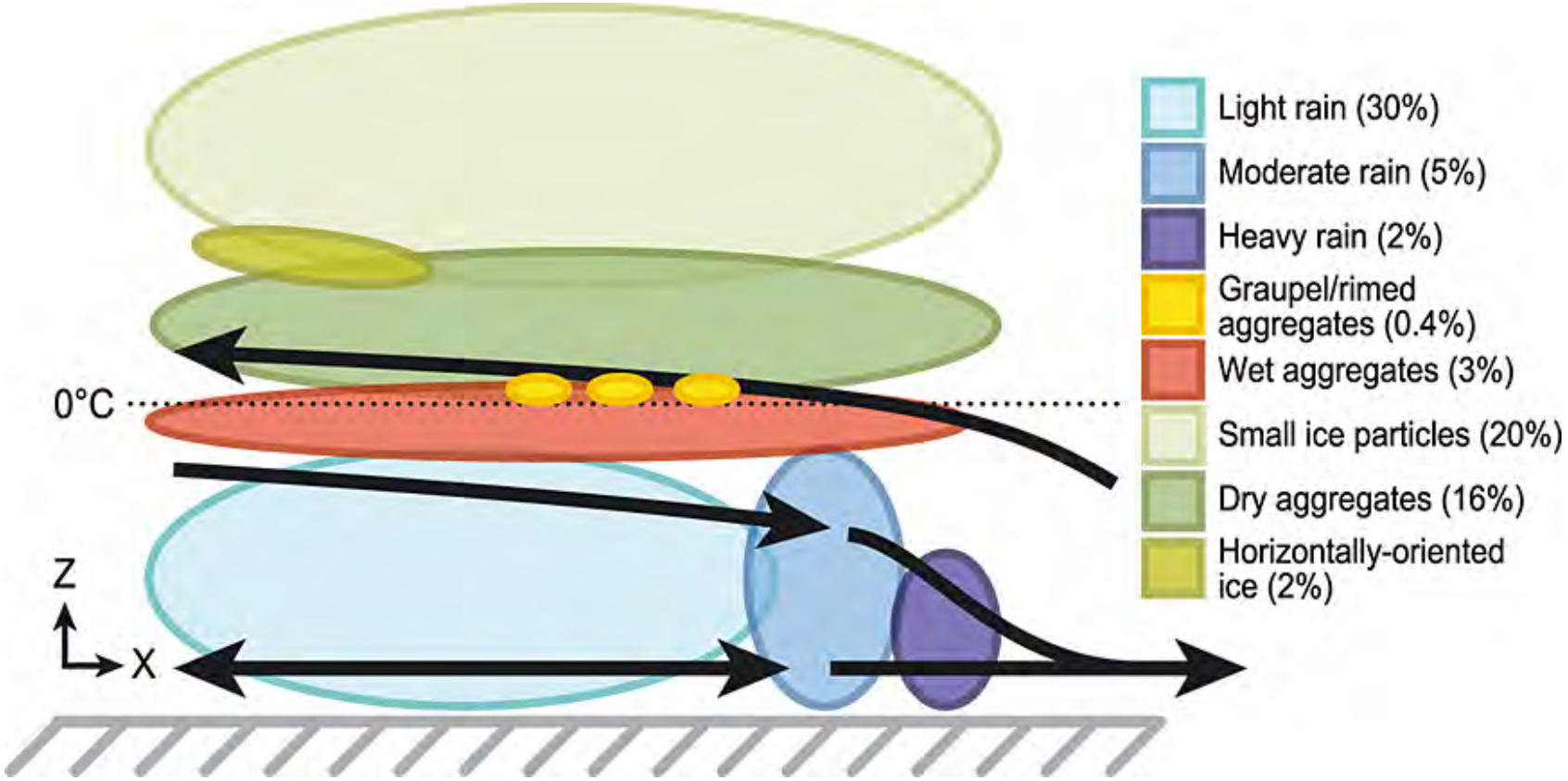

MR3252: Tropical Meteorology

Diurnal Variability

Main Topics:

- Day-night variability in rainfall, surface fluxes, humidity
- Land-sea driven diurnal cycles
- Diurnal cycles in tropical cyclones

Ruppert and Hohenegger (2018)

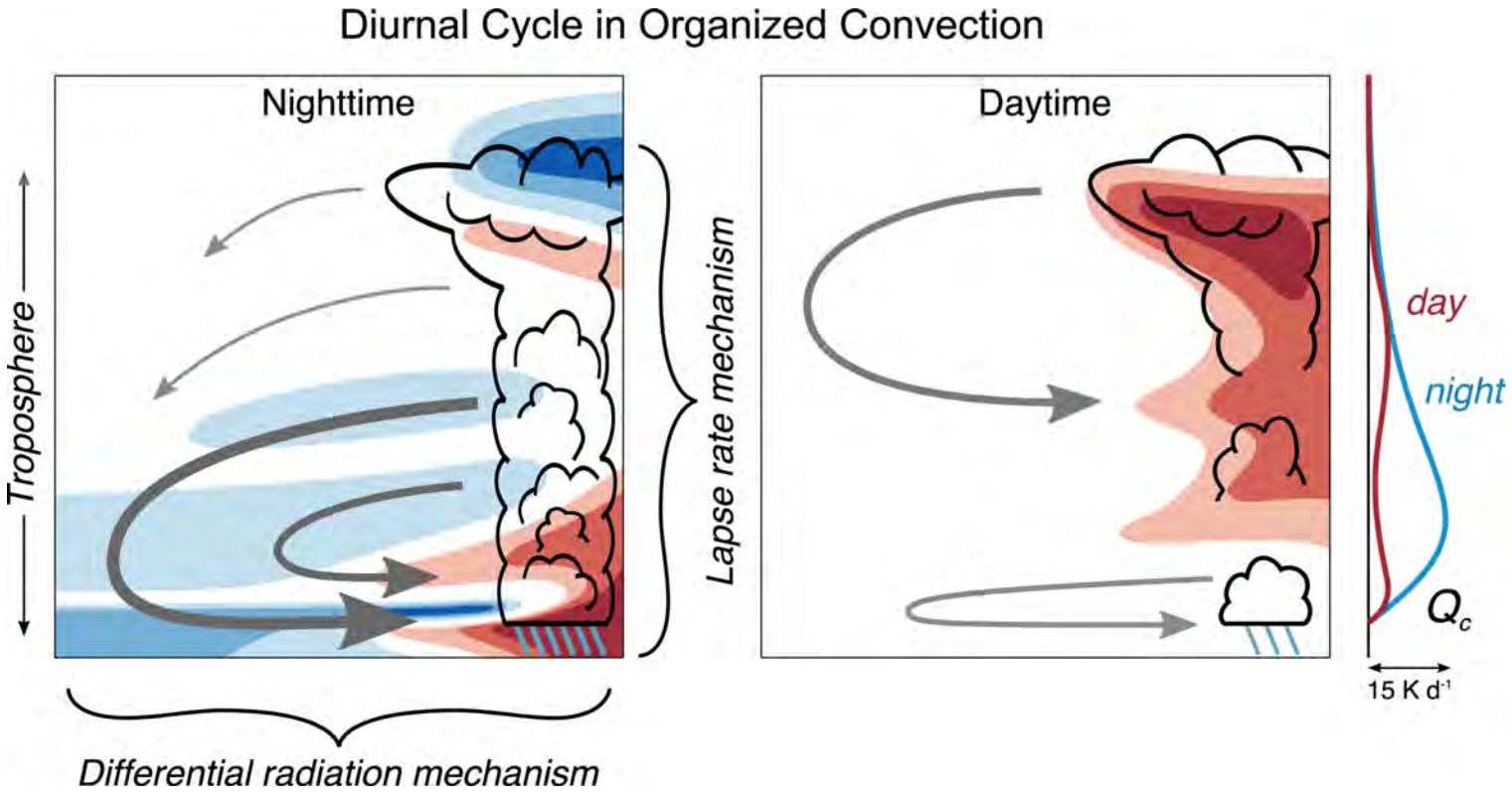

Ruppert and Hohenegger (2018)

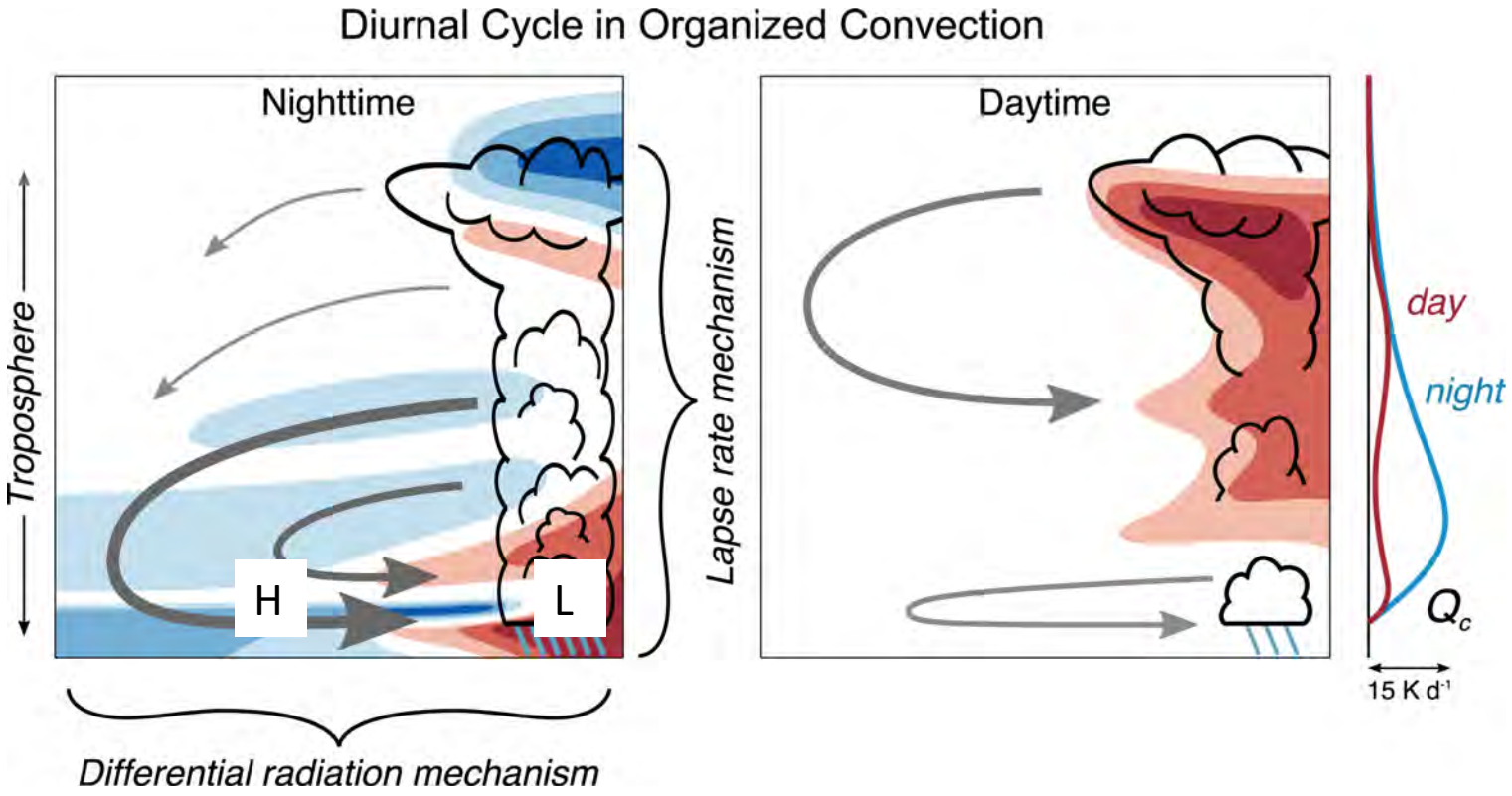

Powell et al. (2012)

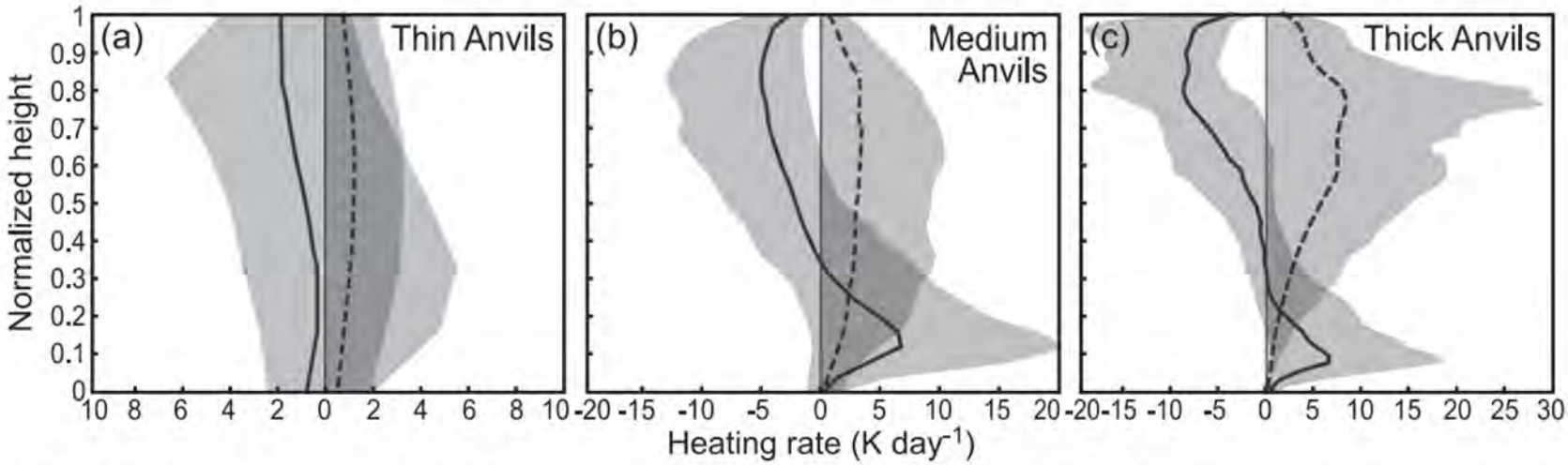

FIG. 5. In-cloud heating rates (K day^{-1}) computed by a radiative transfer code for (a) thin, (b) medium, and (c) thick anvil clouds detected by WACR. Height is normalized, so that the cloud base occurs at 0, and the cloud top occurs at 1. Solid lines depict median longwave (LW) heating rates, and dashed lines represent mean shortwave (SW) heating rates. The shaded area contains the inner 80% of the distribution of heating rates observed at each normalized height. The thin vertical black line represents zero heating.

Sakaeda et al. (2018)

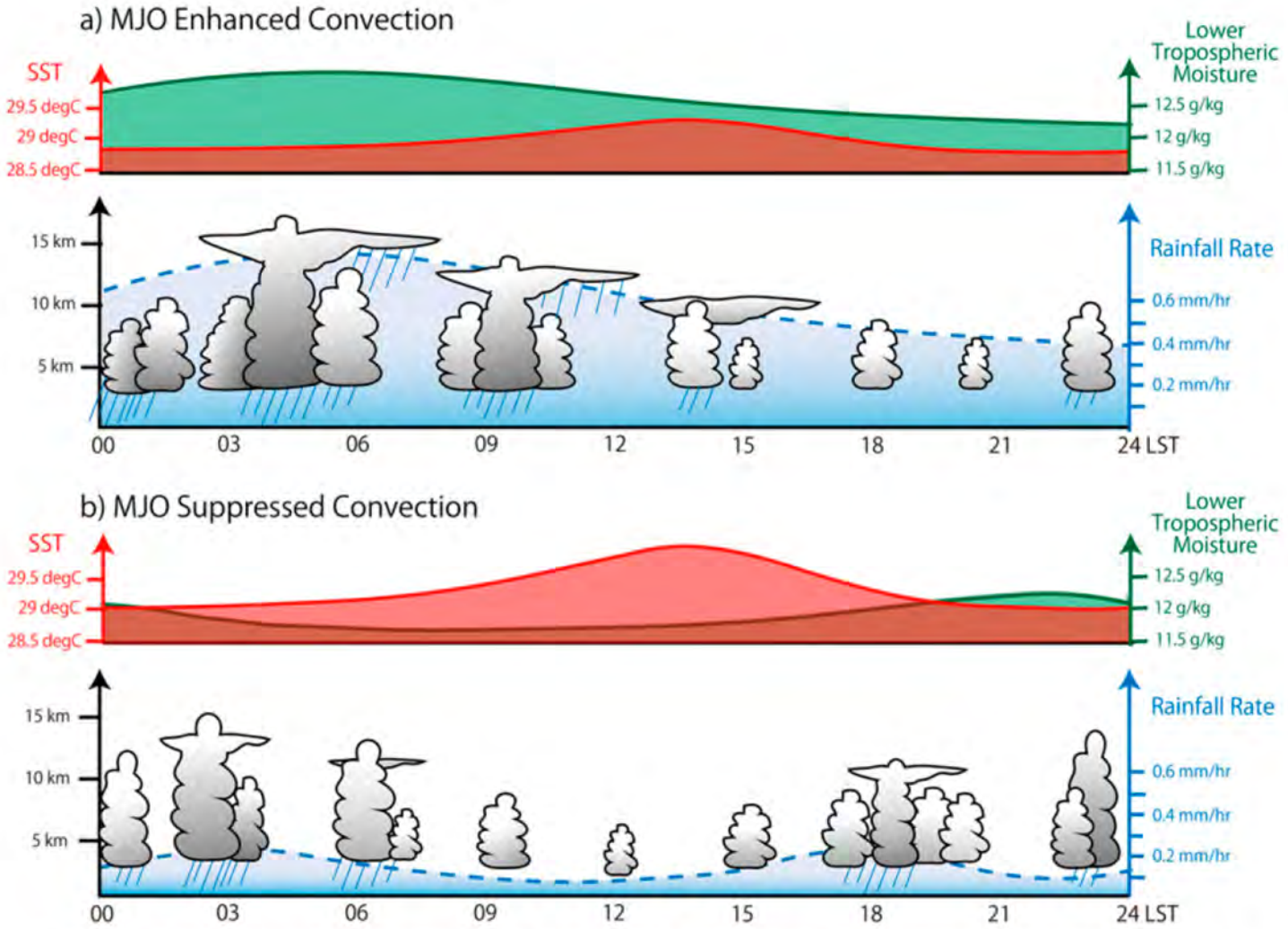

FIG. 9. Schematic of the diurnal cycle of rainfall, clouds, lower-tropospheric moisture, and SST during the MJO (a) enhanced and (b) suppressed phases during the DYNAMO field campaign. Green and red shading at the top of each panel represent the diurnal variability of lower-tropospheric (averaged from 700 to 1000 hPa) water vapor mixing ratio and SST. Blue lines at the bottom of each panel represent the diurnal variability of total rainfall over the area covered by the S-Polka radar. Tall clouds indicate convective and accompanying wide thin clouds represent stratiform–anvil clouds. Other shallower clouds represent those associated with isolated convective rain.

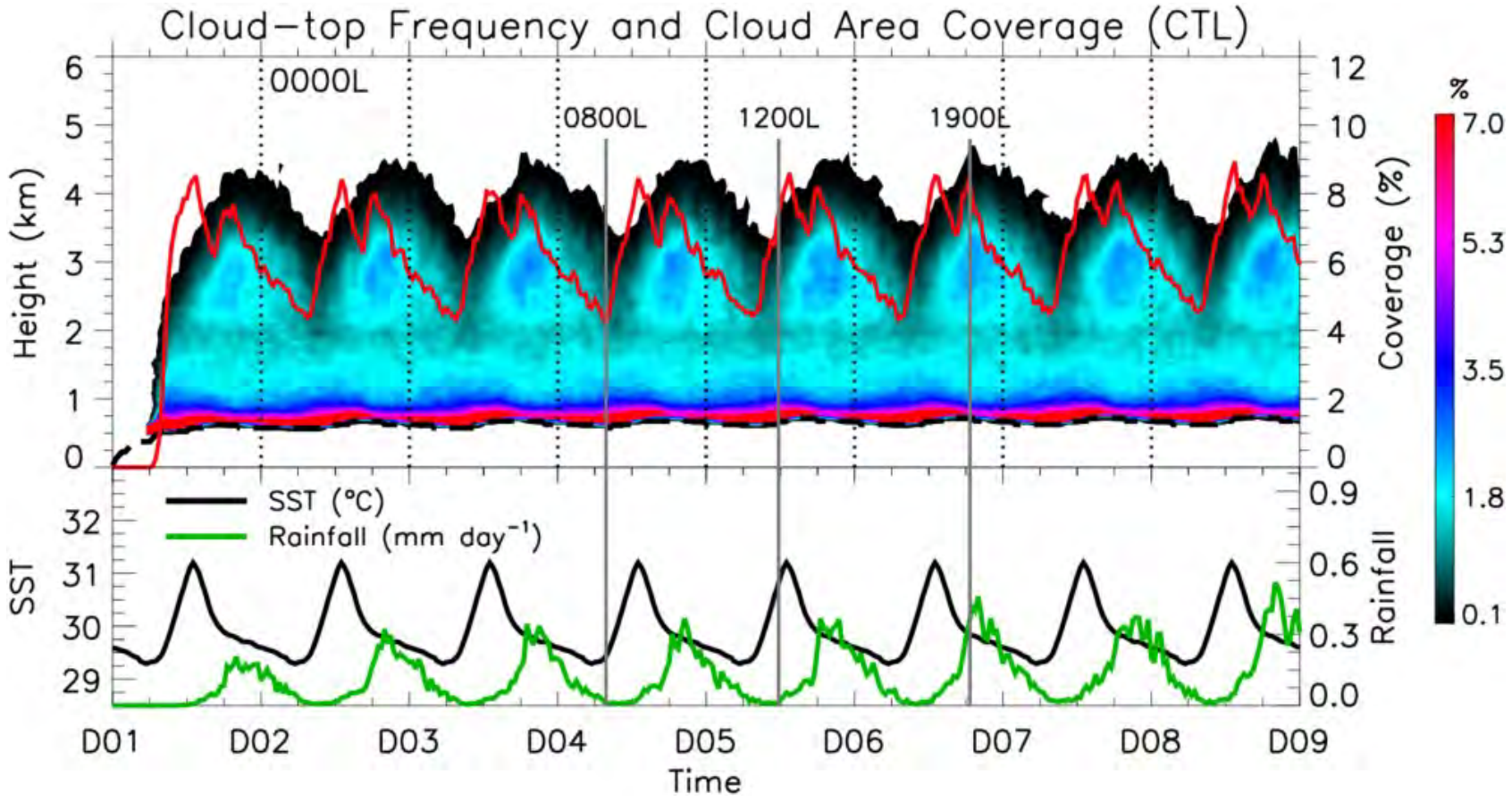
Cloud–top Frequency and Cloud Area Coverage (CTL)
0000L
0800L
1200L
1900L
Height (km)
Coverage (%)
%
7.0
5.3
3.5
1.8
0.1
SST (°C)
Rainfall (mm day⁻¹)
SST
Rainfall
D01
D02
D03
D04
D05
D06
D07
D08
D09
Time

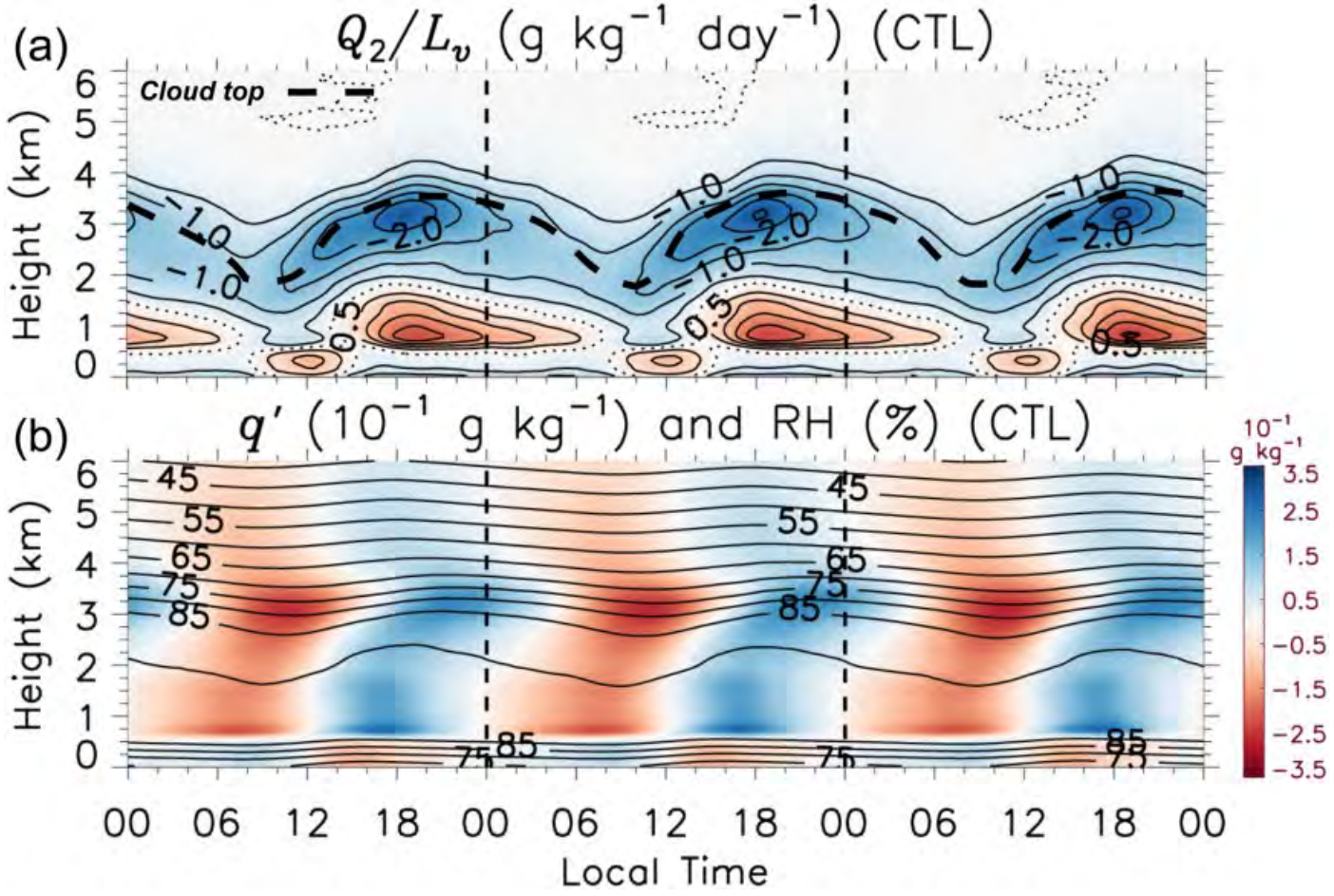
(a)
Q_2/L_v (g kg^{-1} day^{-1}) (CTL)
Cloud top
Height (km)
(b)
q' (10^{-1} g kg^{-1}) and RH (%) (CTL)
10^{-1} g kg^{-1}
Local Time
00 06 12 18 00 06 12 18 00 06 12 18 00

Dunion et al. (2014)

Diurnal pulsing of convection

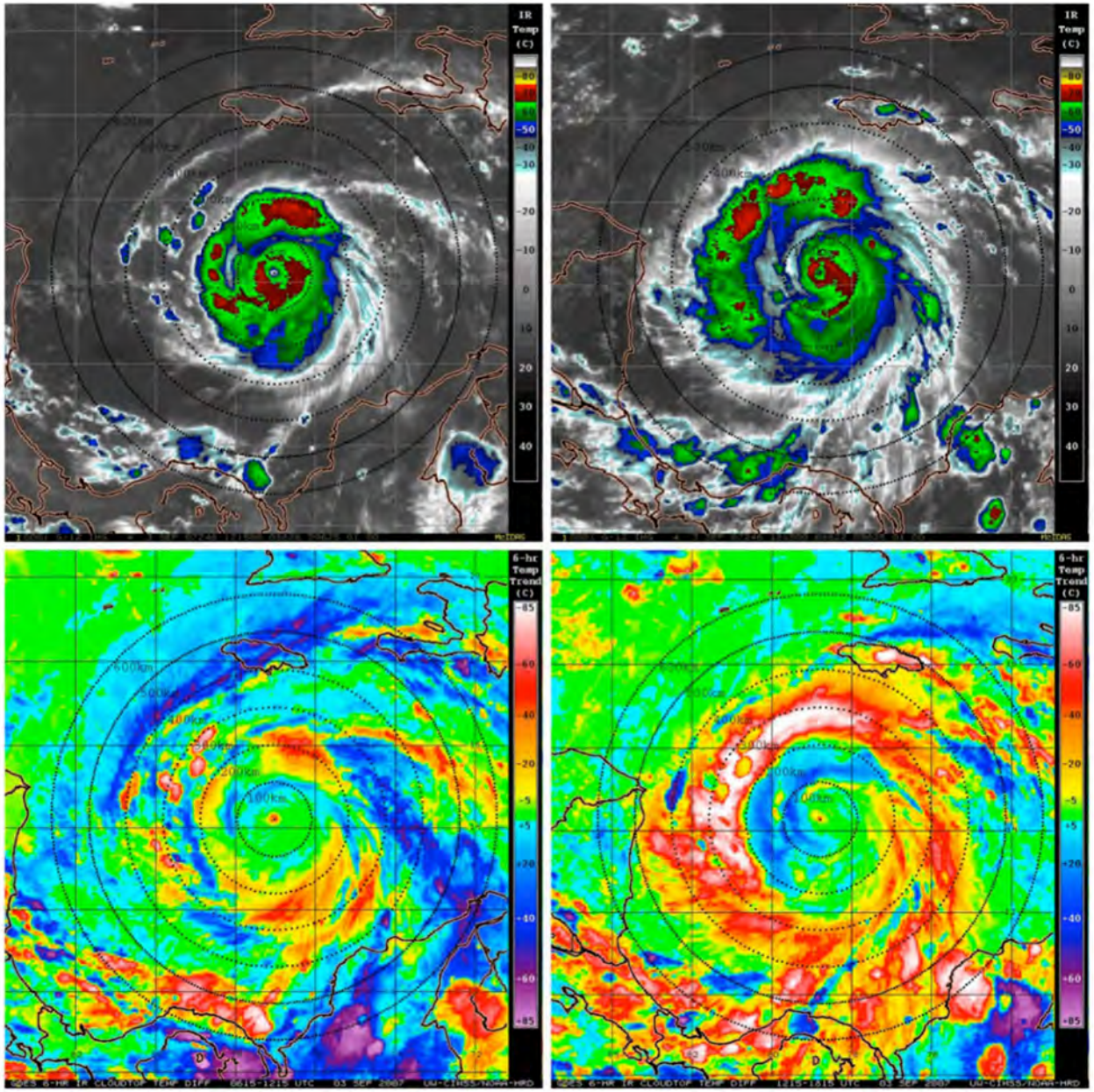

FIG. 1. (top) GOES IR imagery showing 2007 Hurricane Felix valid at (left) 1215 UTC (0715 LST) and (right) 1815 UTC (1315 LST) 3 Sep. (bottom) The corresponding 6-h GOES IR brightness temperature differencing images for these times . The yellow to pink shading (−10° to −85°C IR cooling tendencies) indicates a diurnal pulse propagating away from the storm during this period. The 100–600-km range rings (black dashed curves) from the TC center are overlaid on each of the satellite images. Lines of latitude and longitude are marked at 2° intervals.

Dunion et al. (2014)

Diurnal pulsing of convection

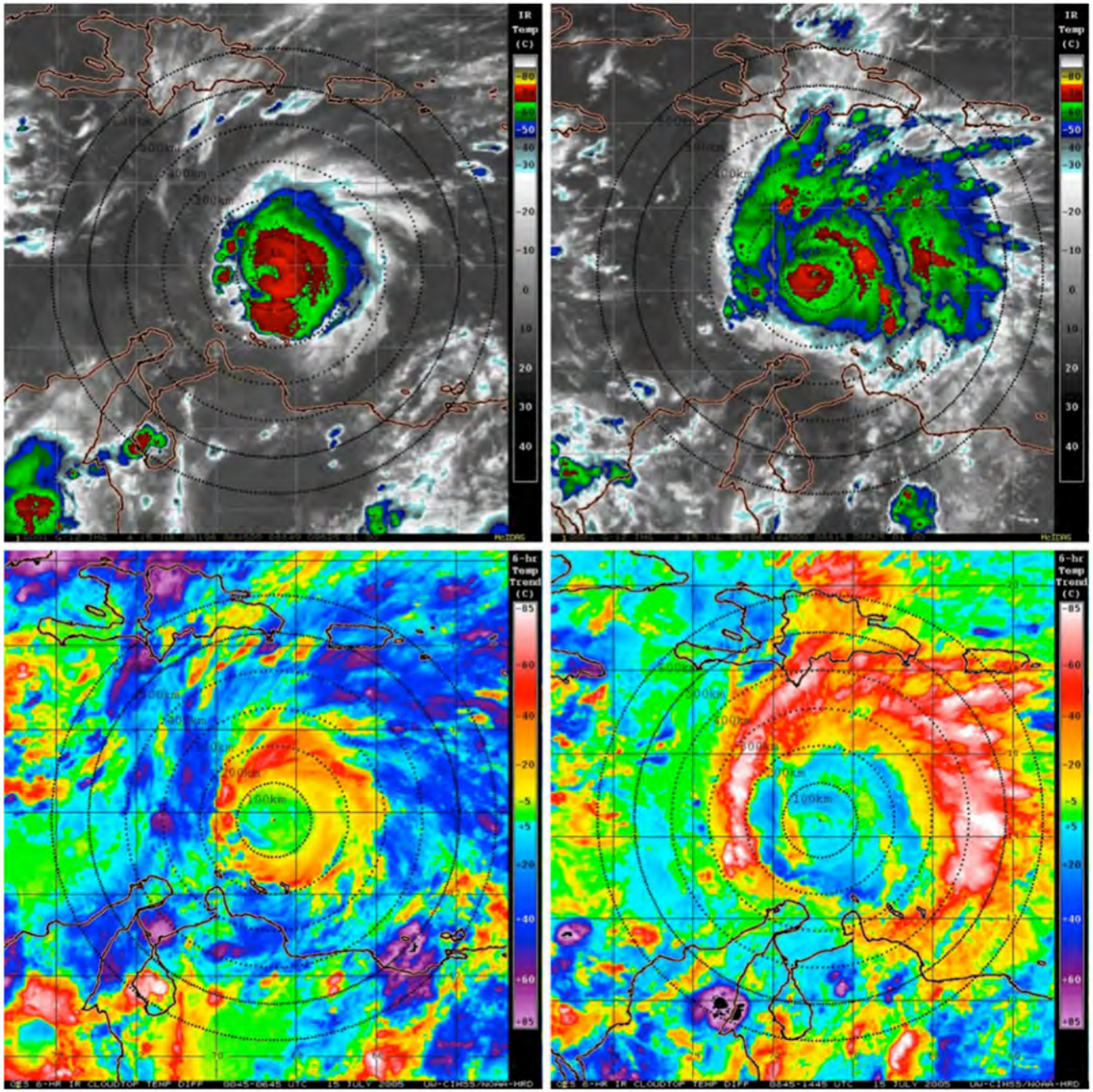

FIG. 4. As in Fig. 1, but for 2005 Hurricane Emily valid for (left) 0645 UTC (0145 LST) and (right) 1445 UTC (0945 LST) 15 Jul.

Kossin (2002)

Diurnal cycle in TCs

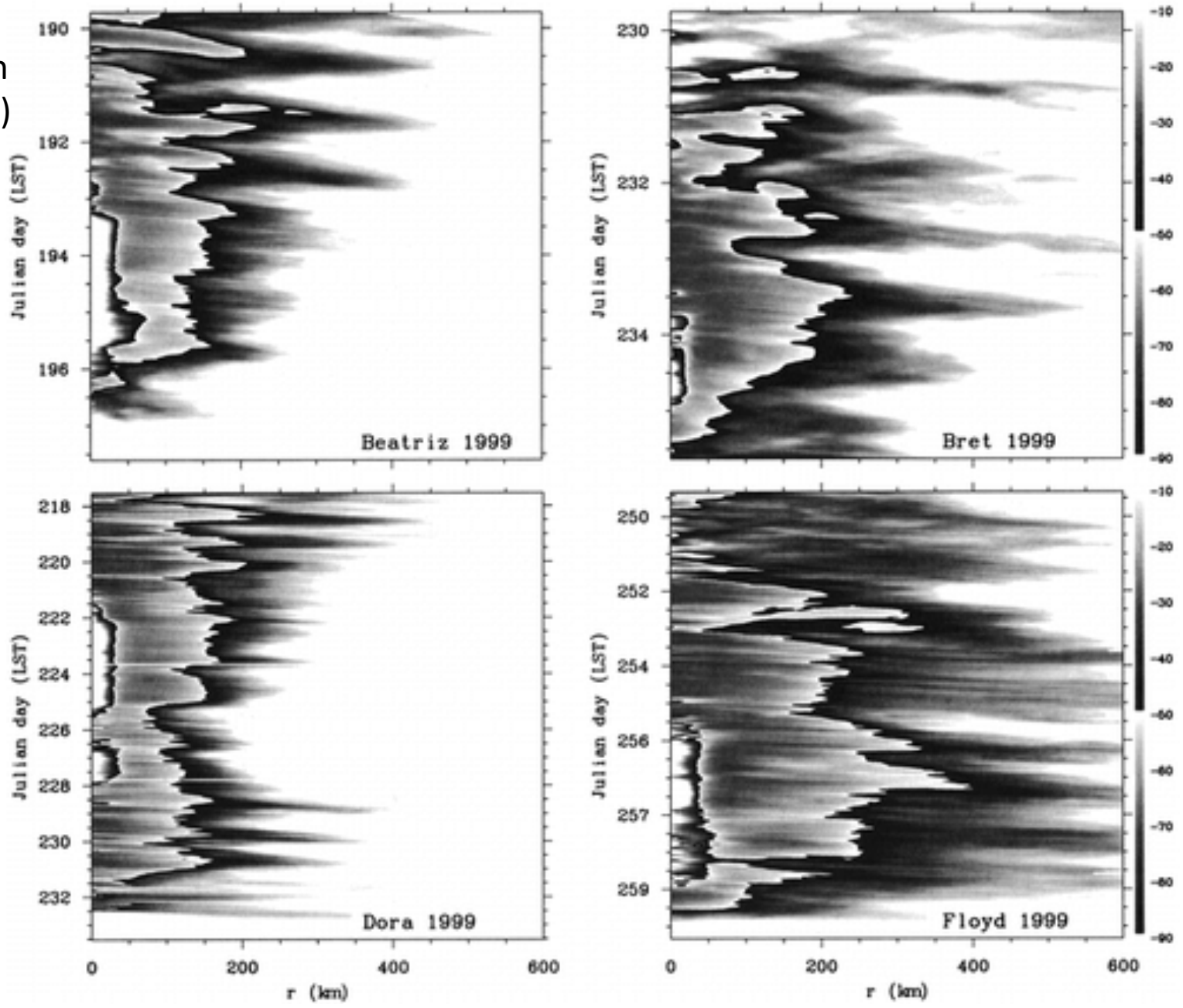

Kossin (2002)

Diurnal cycle in TCs

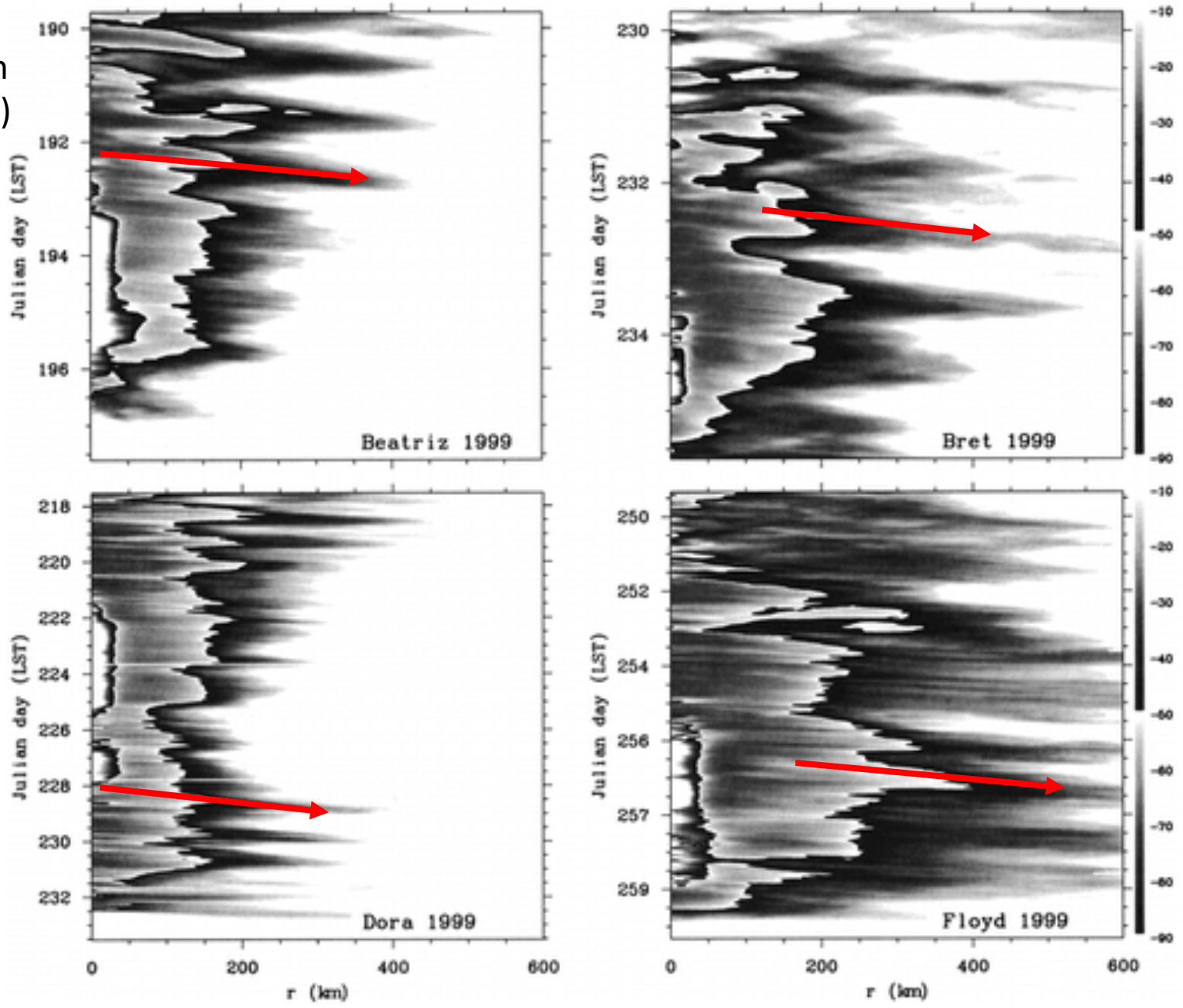

Ruppert and O'Neill (2019)

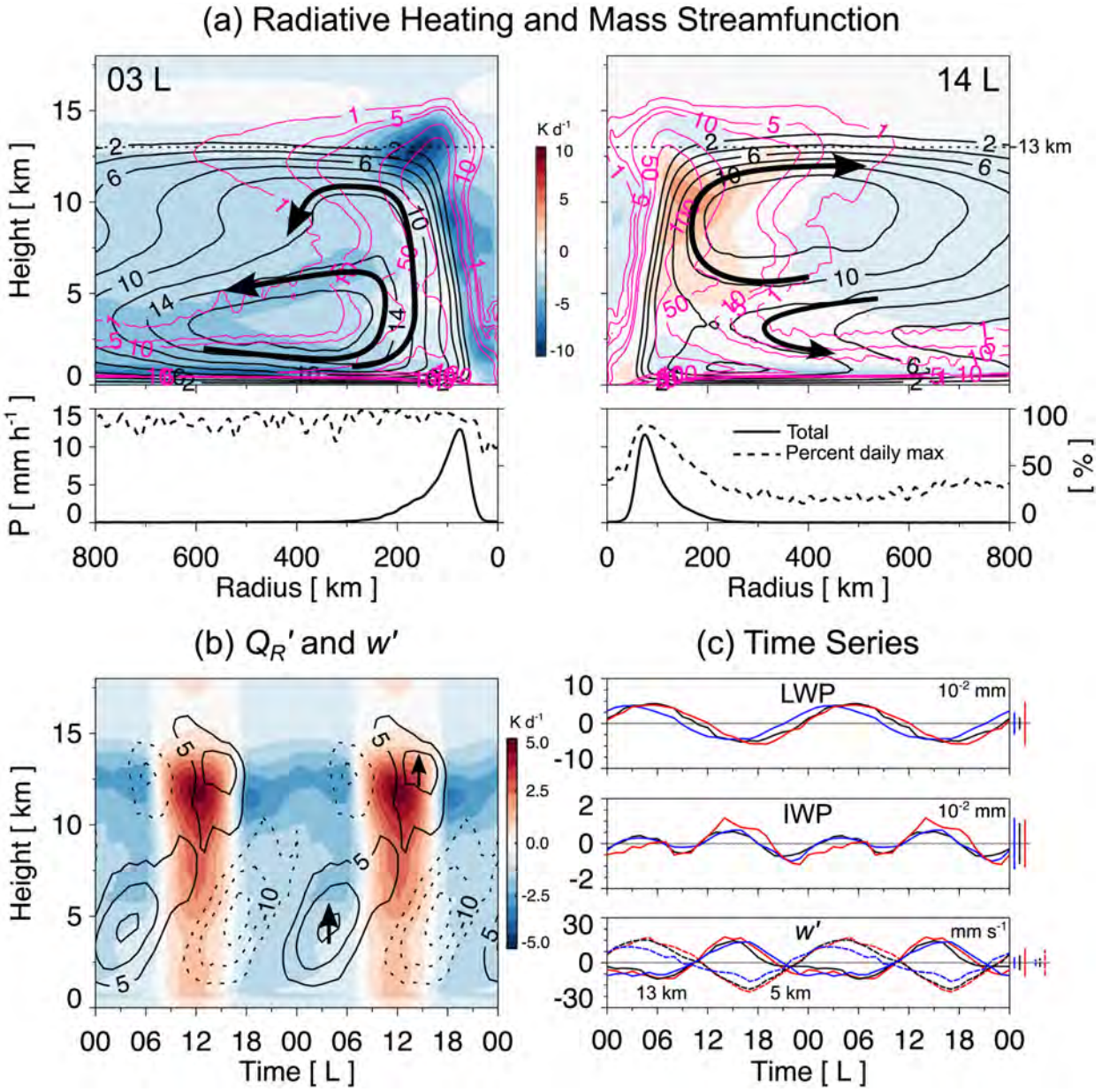

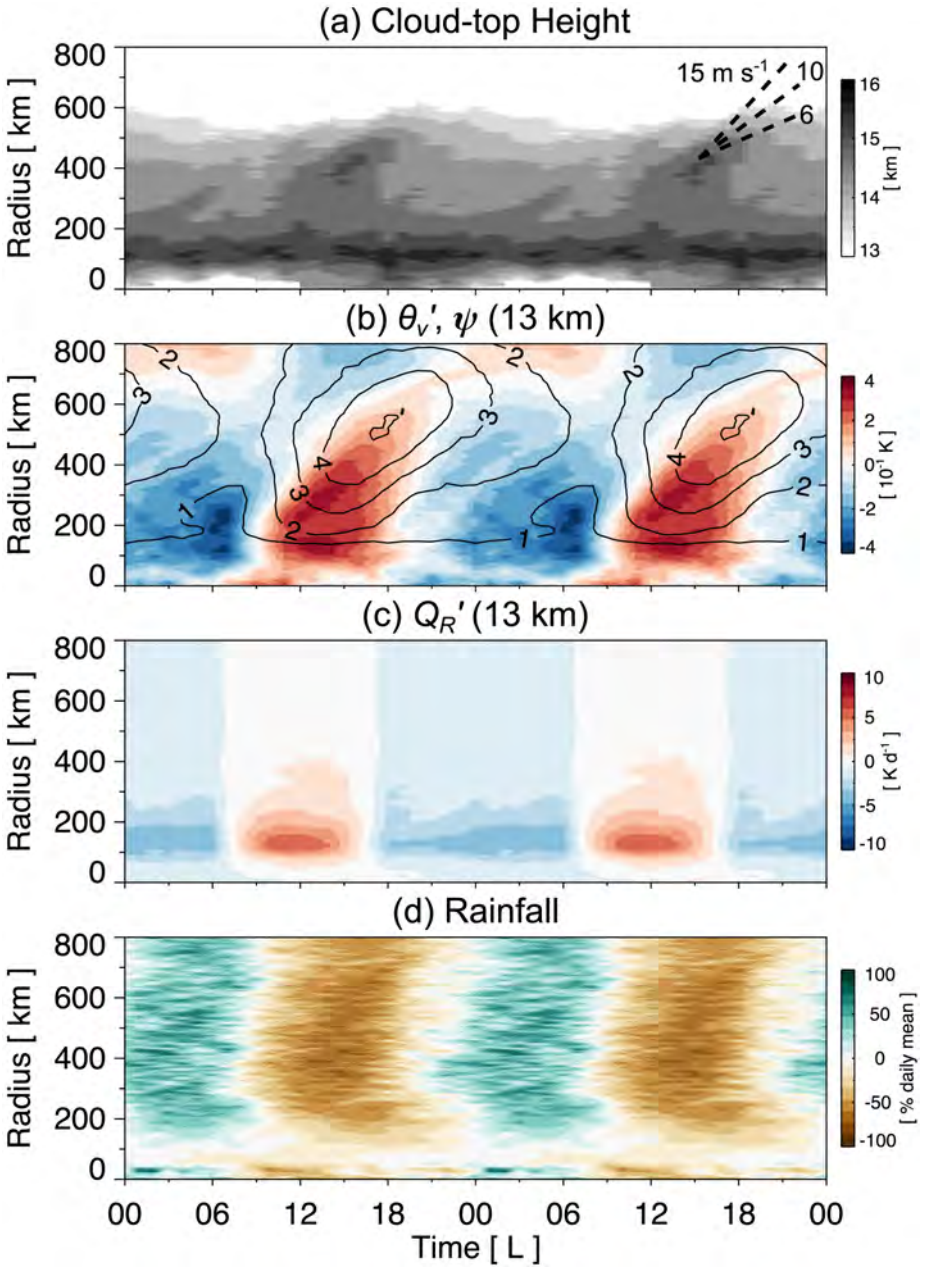
(a) Cloud-top Height
15 m s-1
10
6
16
15
14
13
[km]
Radius [km]
800
600
400
200
0
(b) θv′, ψ (13 km)
4
2
0
-2
-4
[10-1 K]
(c) QR′ (13 km)
10
5
0
-5
-10
[K d-1]
(d) Rainfall
100
50
0
-50
-100
[% daily mean]
00
06
12
18
00
06
12
18
00
Time [L]

Natoli and Maloney (2019)

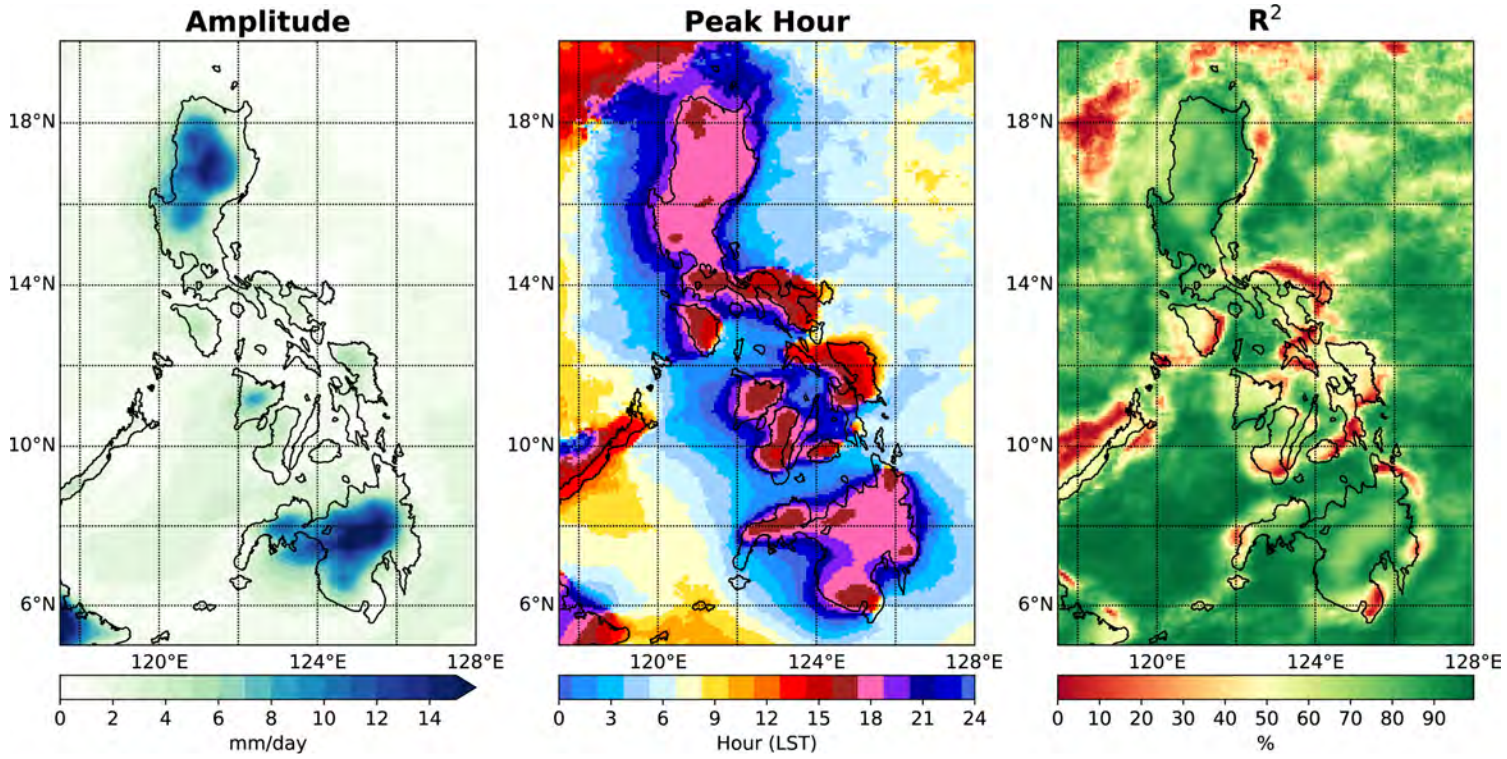

From CMORPH precipitation, (a) the amplitude of the first diurnal harmonic of the boreal summer composite diurnal cycle, (b) its peak hour (LST), and (c) the variance in the boreal summer composite diurnal cycle explained by the first diurnal harmonic.

Peatman et al (2014)

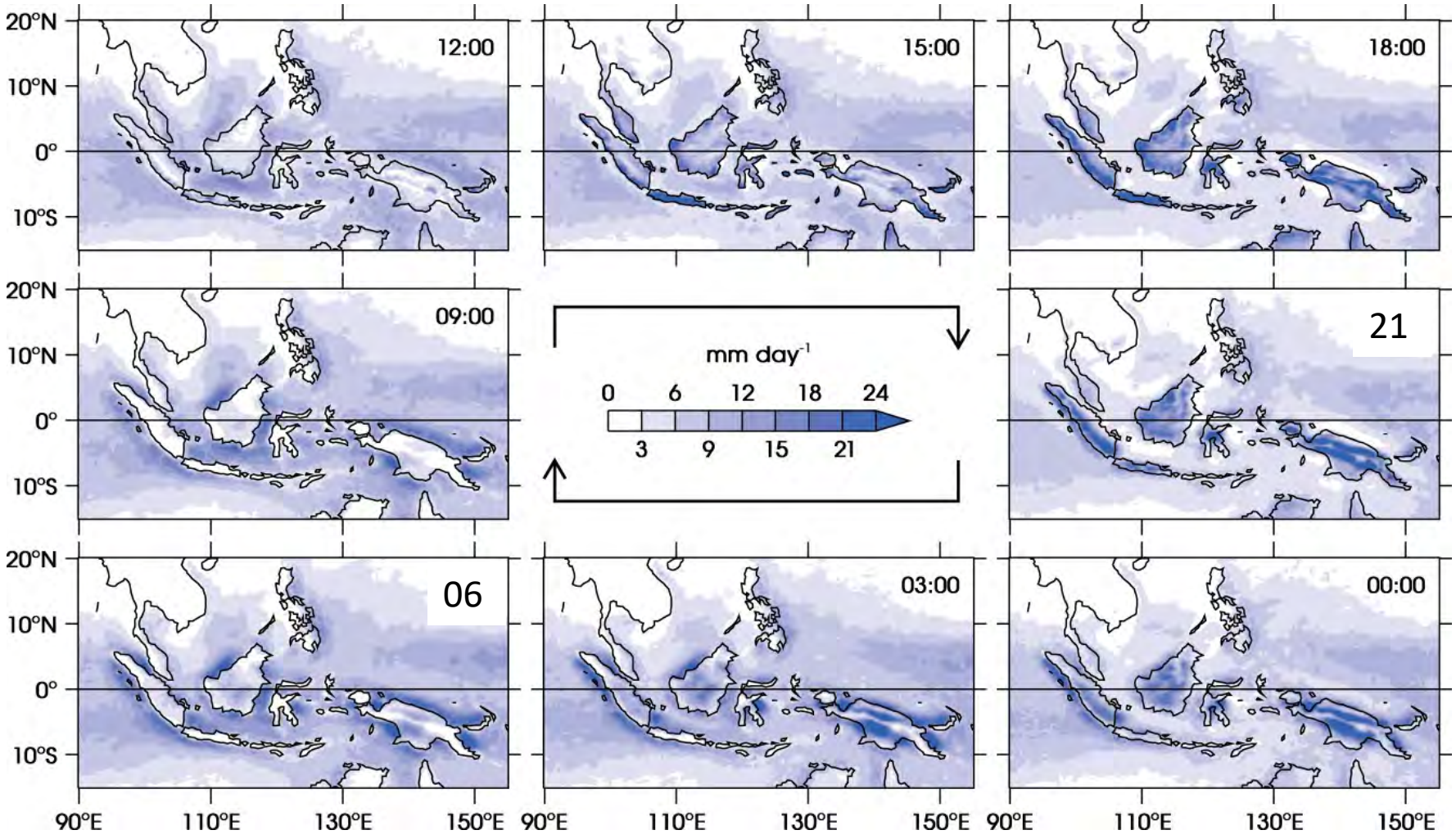

MR3252: Tropical Meteorology

Cold Pools

Main Topics:

- Structure and dynamics of convectively driven cold pools

Droegemeier and Wilhelmson (1987)

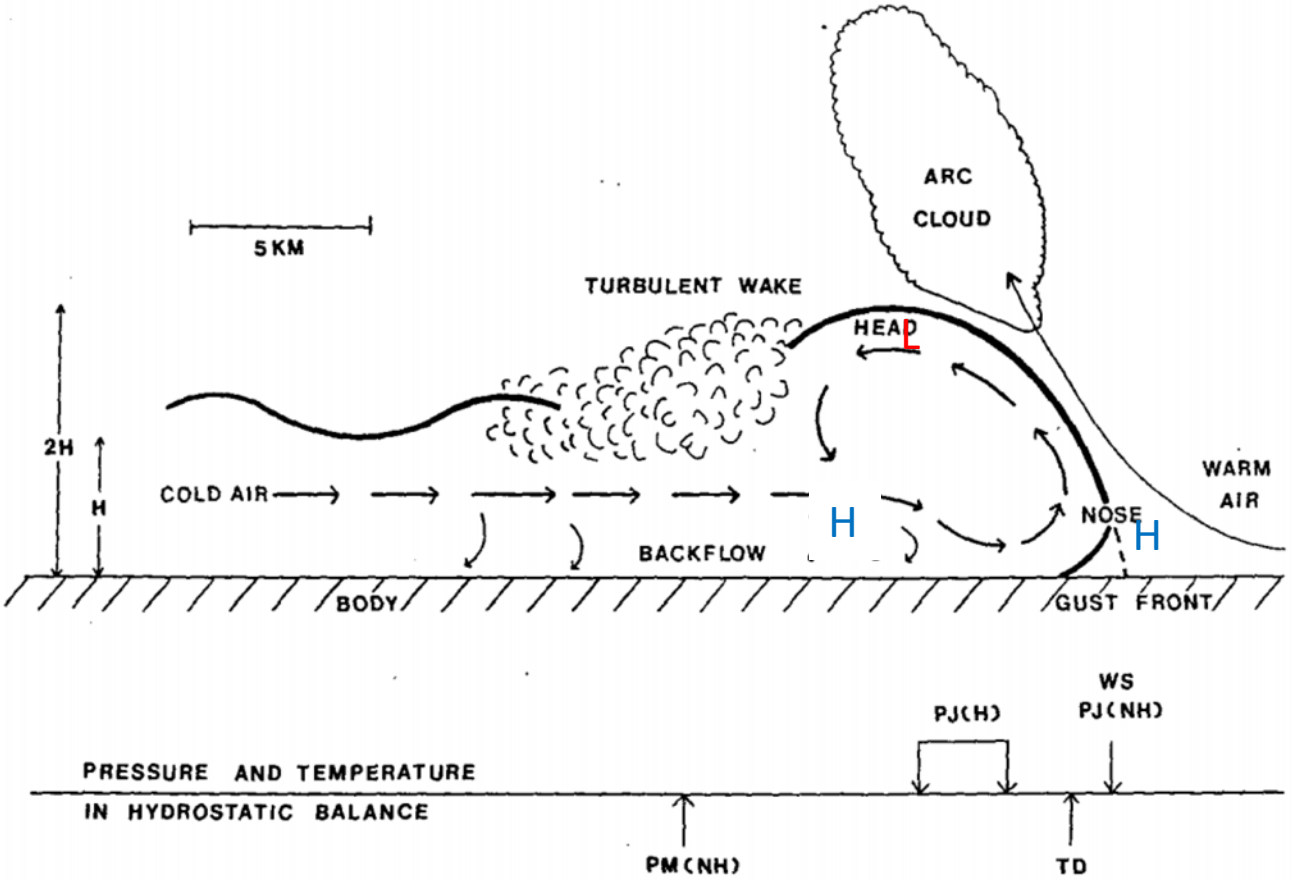

FIG. 1. Schematic vertical cross section through a mature thunderstorm outflow (vertical scale exaggerated), and the corresponding changes in surface meteorological parameters. See the text for details. (Adapted from Charba, 1974; Goff, 1975; Wakimoto, 1982; Koch, 1984).

Cold Pools

Forward advance of gravity currents driven by pressure gradient force. In a 2D cross-section:

$$\frac{Du}{Dt} = -\frac{1}{\rho_o}\frac{\partial p'}{\partial x} \quad \xrightarrow{\text{Steady state following gust front}} \quad \frac{\partial (u^2/2)}{\partial x} = -\frac{1}{\rho_o}\frac{\partial p'}{\partial x}$$

Integrate the above equation for a gravity current with depth h and a density of $\rho_o + \rho = \Delta\rho$ in a background wind of zero to get the velocity of the cold pool, *U*.

$$U = \sqrt{2gh\left(\frac{\Delta\rho}{\rho_o}\right)}$$

Therefore, the density difference between the low θ_e air and the high θ_e air on either side of the cold pool boundary—as well as the cold pool depth—affect the propagation speed.

From here: $\frac{Du}{Dt} = -\frac{1}{\rho_o}\frac{\partial p'}{\partial x}$ Let u $= \frac{Dx}{Dt}$ and $\frac{1}{Dt} = \frac{u}{Dx}$ to get

$$\frac{D}{Dx}\left(\frac{u^2}{2} + \frac{p'}{\rho_0}\right) = 0$$

Then integrate ahead of gust front (from some distance well ahead of gust front where u=0 and p'=0) to the gust front, then:

$$p' = \frac{\rho_0 U^2}{2}$$

This means that the horizontal kinetic energy (U^2) is converted to enthalpy at the gust front, but the pressure perturbation is not hydrostatically driven (i.e. driven by buoyant motions). A dynamic contribution to the pressure perturbation exists.

Recall from the 3D momentum equation (with friction and Coriolis = 0) with an anelastic assumption:

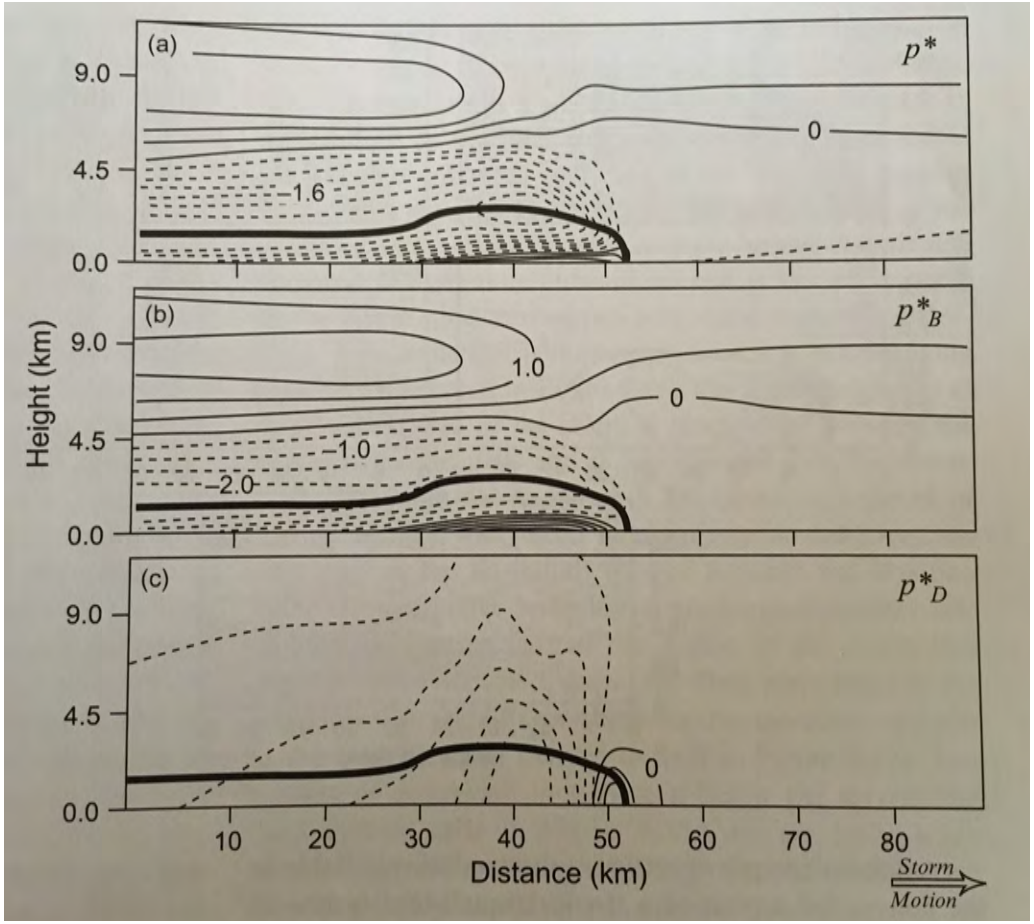

Fovell and Ogura (1988), adapted from Houze (2014)

$$\nabla^2 p' = \frac{\partial}{\partial z}(\rho_0 B) + -\nabla \cdot (\rho_0 \mathbf{v} \cdot \nabla \mathbf{v})$$

Buoyancy pressure perturbation

Dynamic pressure perturbation

Feng et al. (2015): Schematic of isolated cold pools and intersecting cold pools

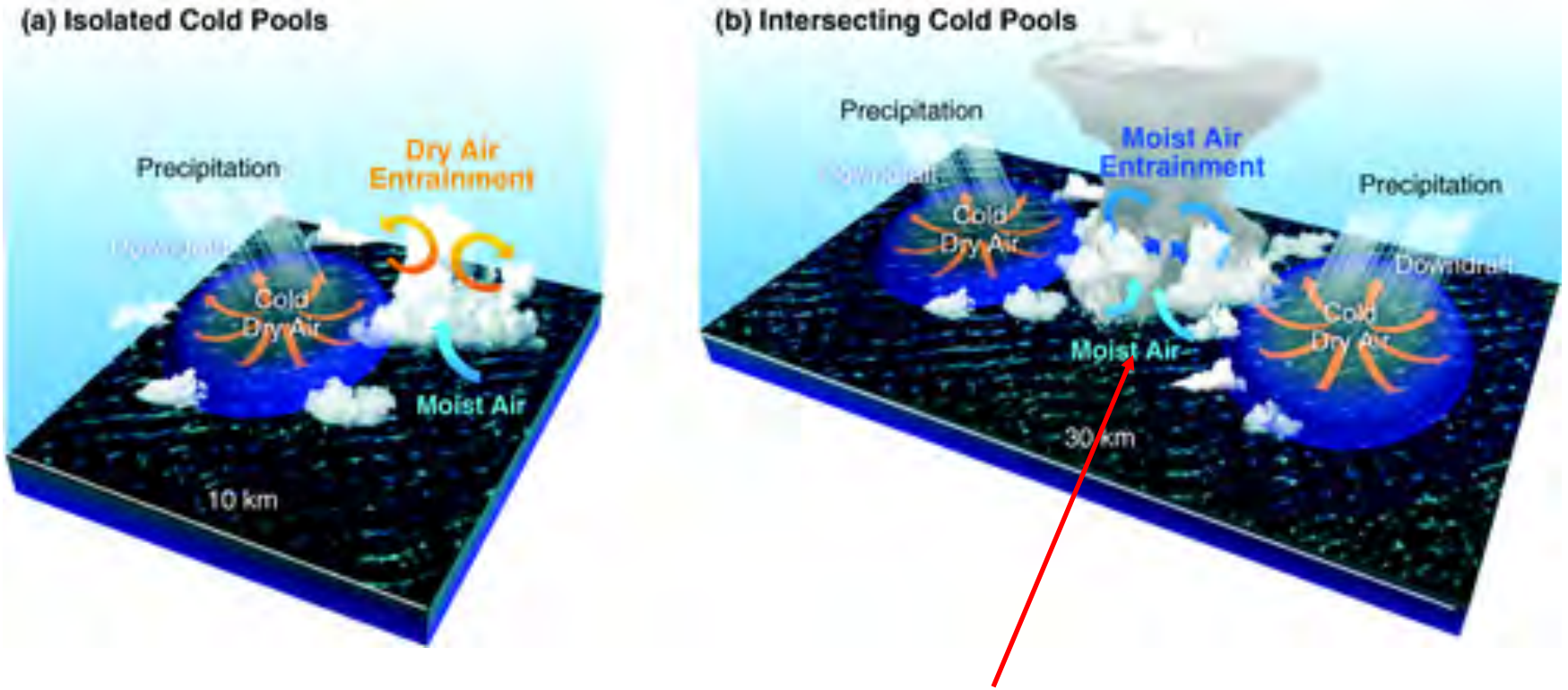

Enhanced low-level convergence in a more moist environment

Modeled updraft velocities at cold pool boundaries for 2-hour-old cold pools

Feng et al. (2015)

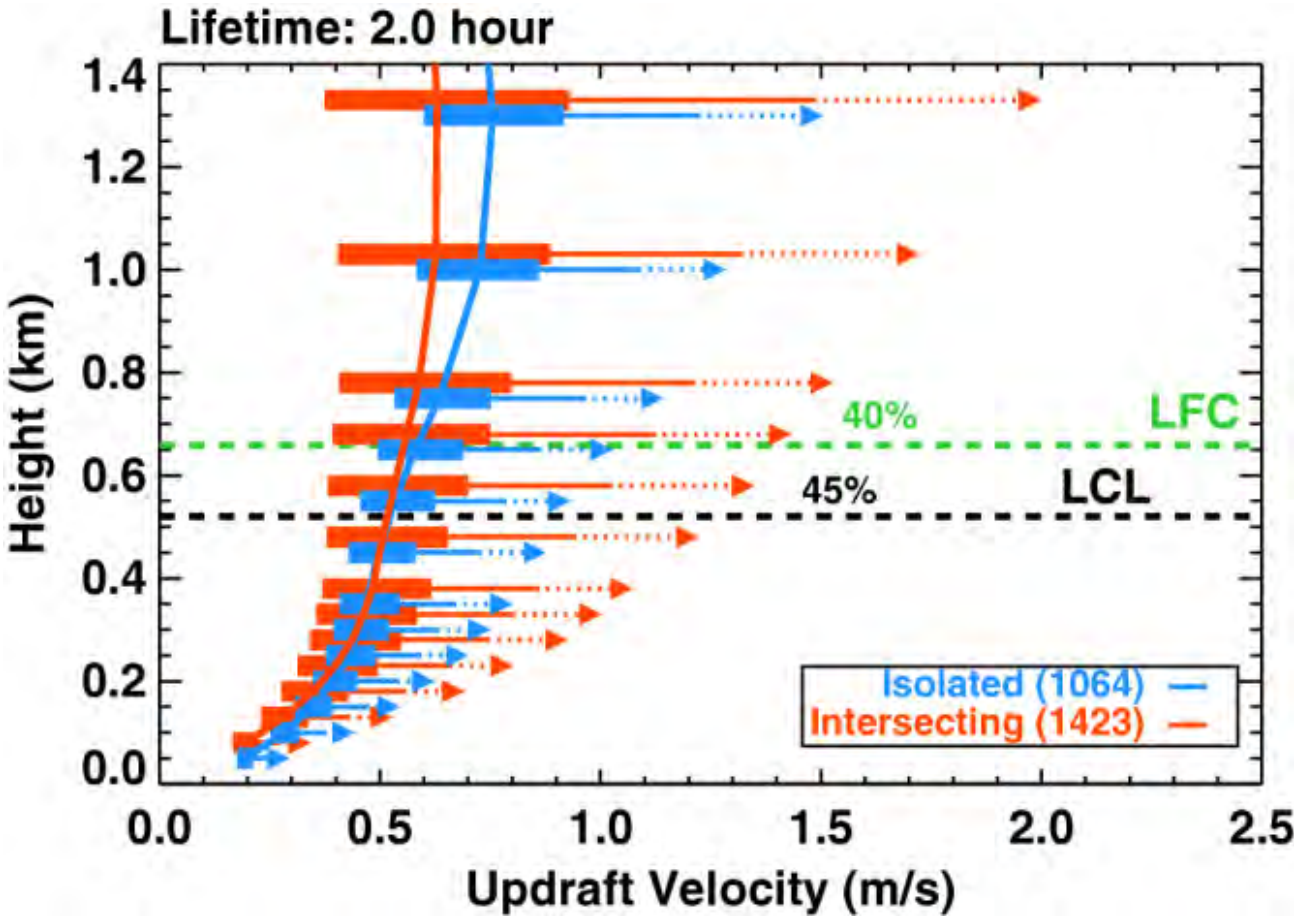

Feng et al. (2015)

Cold pools in radar observations